

Dissipative Locally Resonant Metasurfaces for Low-Frequency Rayleigh Wave Mitigation

Siqi Wang^{a,b}, Zhigang Cao^{a,c,*}, Shaoyun Wang^b, Qian Wu^b, Jiaji Chen^b, Yuanqiang Cai^a, Guoliang Huang^{d,*}

^a*Department of Civil Engineering and Architecture, Zhejiang University, Hangzhou 310058, China*

^b*Department of Mechanical and Aerospace Engineering, University of Missouri, Columbia, MO 65211, USA*

^c*Center for Balance Architecture, Zhejiang University, Hangzhou 310058, China*

^d*Department of Mechanics and Engineering Science, Peking University, Beijing, 100871, China*

Abstract

Low-frequency Rayleigh waves from earthquakes, traffic, or heavy machinery pose significant risks to engineering structures, and how to mitigate subwavelength Rayleigh waves is a major challenge in the field. While attaching non-dissipative local resonators to the surface is a potential solution, its effectiveness is typically confined to narrow frequency ranges. This study proposes an elastic dissipative metasurface (EDM) for broadband mitigation and absorption, along with an energy analysis based on Poynting's theorem to quantify the wave scattering generated by EDMs. To realize broadband Rayleigh wave mitigation, we propose multi-resonant EDMs, where local resonators produce bandgaps at different frequencies, and damping bridges these gaps into a continuous broad bandgap. The working mechanism of the EMD to suppress broadband Rayleigh waves is revealed in a dissipative mass-in-mass lattice system through both negative effective mass density and effective metadamping coefficient. Furthermore, we design a graded EDM with slow modulation properties that eliminate scattered waves, achieving zero reflection, perfect rainbow absorption, and effective modulation of Rayleigh waves by leveraging the adiabatic theorem. The study can open new opportunities in the development of a new functional metasurface as an efficient wave mitigation material to suppress earthquake waves.

Keywords: Elastic dissipative metasurfaces, Rayleigh wave mitigation, local resonators, perfect rainbow absorption, microstructure design

¹ 1. Introduction

² Mechanical metamaterials are engineered structural materials with mechanical properties
³ rarely observed in natural materials. A hallmark of these materials is local resonance, char-
⁴ acterized by subwavelength locally resonant inclusions or resonators [1, 2, 3, 4, 5]. Typically,

*Corresponding author

Email addresses: caozhigang2011@zju.edu.cn (Zhigang Cao), guohuang@pku.edu.cn (Guoliang Huang)

the degrees of freedom of these local resonators can be eliminated, allowing the background media to be modeled as an effective continuum with frequency-dependent mass densities and elastic moduli [6, 7, 8]. These effective properties can even be negative, leading to unconventional phenomena such as negative refraction [9, 10, 11], wave cloaking [12, 13, 14], and superlensing [15, 16]. The negative properties also create subwavelength bandgaps, providing a promising solution for low-frequency vibration and noise isolation, a challenge for traditional methods [17, 18, 19, 20].

The development of metamaterials has opened new possibilities for surface wave engineering, enabling control over Rayleigh waves generated by sources such as earthquakes, traffic, or heavy machinery. Traditionally, Rayleigh waves are mitigated using open and filled trenches [21, 22, 23, 24], wave barriers [25, 26, 27], piles [28, 29, 30, 31], and dampers [32, 33]. However, these conventional solutions are often bulky and ineffective for isolating low-frequency waves below 20 Hz. By installing resonators on the surface of a semi-infinite medium, it is possible to reduce Rayleigh wave transmission by creating a bandgap in the low-frequency range [34, 35]. This approach has gained attention in various scenarios, including saturated soil substrates [36], stratified substrates [37, 38], buried resonators [39, 40], double resonators [41, 42], and nonlinear resonators [42, 43, 44]. However, local resonance generates significant bulk waves and reflected Rayleigh waves, presenting unforeseen challenges. The impact of local resonance on Rayleigh wave scattering, as well as strategies to eliminate these unintended waves, remains unclear. Moreover, the development of an effective theory for multiple local resonances has not been reported, nor has the influence of negative effective mass function on surface wave decaying been thoroughly explored.

In addition to local resonances, damping significantly influences wave attenuation in materials, as it dissipates wave energy during propagation [45]. Local resonators with a small damping effect can reduce the amplitude of local resonance, decreasing reflection and enhancing wave transmission, while those with a large one can dissipate the wave energy, reducing transmission [42, 46, 47]. When Rayleigh waves pass through the semi-infinite medium with damped resonators, damping has a complex effect on wave scattering due to the existence of multiple wave types. This paper investigates the impact of damping in resonators on wave conversion and presents an energy analysis framework to reveal energy transformation patterns influenced by damping. Furthermore, multiple resonators can generate multiple subwavelength bandgaps [46], and significant damping can broaden the Rayleigh wave attenuation frequency range near these bandgaps [47]. The combination of multiple resonances and damping enables broad-frequency wave attenuation, a technique previously demonstrated for longitudinal waves [47, 48]. Here, we extend this approach to the Rayleigh wave system, achieving broad frequency attenuation with multiple damped resonators. Additionally, we introduce an effective metadamping coefficient to characterize the decay behavior using effective theory.

Uniform arrays of damped local resonators on the half space are unable to fully eliminate reflected surface and bulk waves. To address the issue, a slowly space-varying structure is adopted. The field of space-varying or time-varying systems is emerging in science and engineering [49, 50, 51]. Novel phenomena in Rayleigh wave behavior have been observed using various spring-mass resonators and continuous resonant inclusions on substrate surfaces.

48 For instance, non-reciprocal Rayleigh wave propagation has been achieved with space-time
49 modulated springs, and the conversion of surface waves to shear waves and temporal rain-
50 bow trapping has been realized with time-varying springs [52, 53]. Additionally, topological
51 edge modes and topological pumping of surface waves have been accomplished using space-
52 varying springs [54, 55, 56, 57], and rainbow trapping for surface waves has been achieved
53 using spatially varying resonators [58, 59]. In this study, we extend this concept to perfect
54 rainbow absorption by employing slowly space-varying damped resonators and further de-
55 velop a rigorous theoretical framework for designing such resonators based on the adiabatic
56 theorem [57]. Traditional unit cell analysis based on Bloch's theorem is commonly used to
57 predict wave behavior in periodic systems. However, this approach is inadequate for space-
58 varying systems [57]. Under adiabatic conditions, we leverage the adiabatic theorem and
59 develop a local unit cell analysis method to predict wave behaviors in finite space-varying
60 structures in both frequency and time domains.

61 In this paper, we focus on mitigating the impact of low-frequency Rayleigh waves and
62 scattered waves using elastic dissipative metasurfaces (EDMs) within a broadband frequency
63 range. In Section 2, a semi-infinite elastic substrate with multiple attached resonators is
64 simplified to a substrate with a single effective damped resonator using the effective theory.
65 Subsequently, we develop a framework for calculating the dispersion relations of Rayleigh
66 waves in this substrate incorporating the effective damped resonator. In Section 3, the results
67 of the mitigation effect of EDMs with single resonance on Rayleigh waves are presented,
68 exploring the impact of damping on complex bandgap structures, mode shapes, transmission
69 spectra, conversion patterns, and wave field. Meanwhile, an energy analysis framework is
70 established based on Poynting's theorem to quantify wave scattering from EDMs. In Section
71 4, we extend the analysis to EDMs featuring multiple resonators, achieving broad frequency
72 range wave attenuation. Here, the effective mass and metadamping coefficients derived from
73 the effective theory are used to efficiently characterize the decay behavior of Rayleigh waves,
74 while the microstructure is determined through inverse design. In Section 5, Rayleigh wave
75 behaviors in slowly space-varying EDMs are investigated to achieve the perfect rainbow
76 absorption of all scattered waves. Additionally, a local unit cell analysis method based on
77 the adiabatic theorem is developed to predict wave behavior in these structures. The paper
78 concludes with final remarks and a summary of our findings in Section 6.

79 2. Models and Methods

80 To mitigate the propagation of Rayleigh waves on the ground, we employ novel EDMs
81 composed of dissipative local resonators arranged on the soil surface, as illustrated in Fig.
82 1(a). The energy of the incident Rayleigh waves is distributed among four destinations: the
83 energy of reflected Rayleigh waves, the energy of transmitted Rayleigh waves, the energy
84 of bulk waves, and the energy absorbed by the EDMs. The objective of this study is to
85 design EDMs that mitigate the influence of all scattered waves on infrastructures both on
86 and below the surface, as depicted in Fig. 1(a).

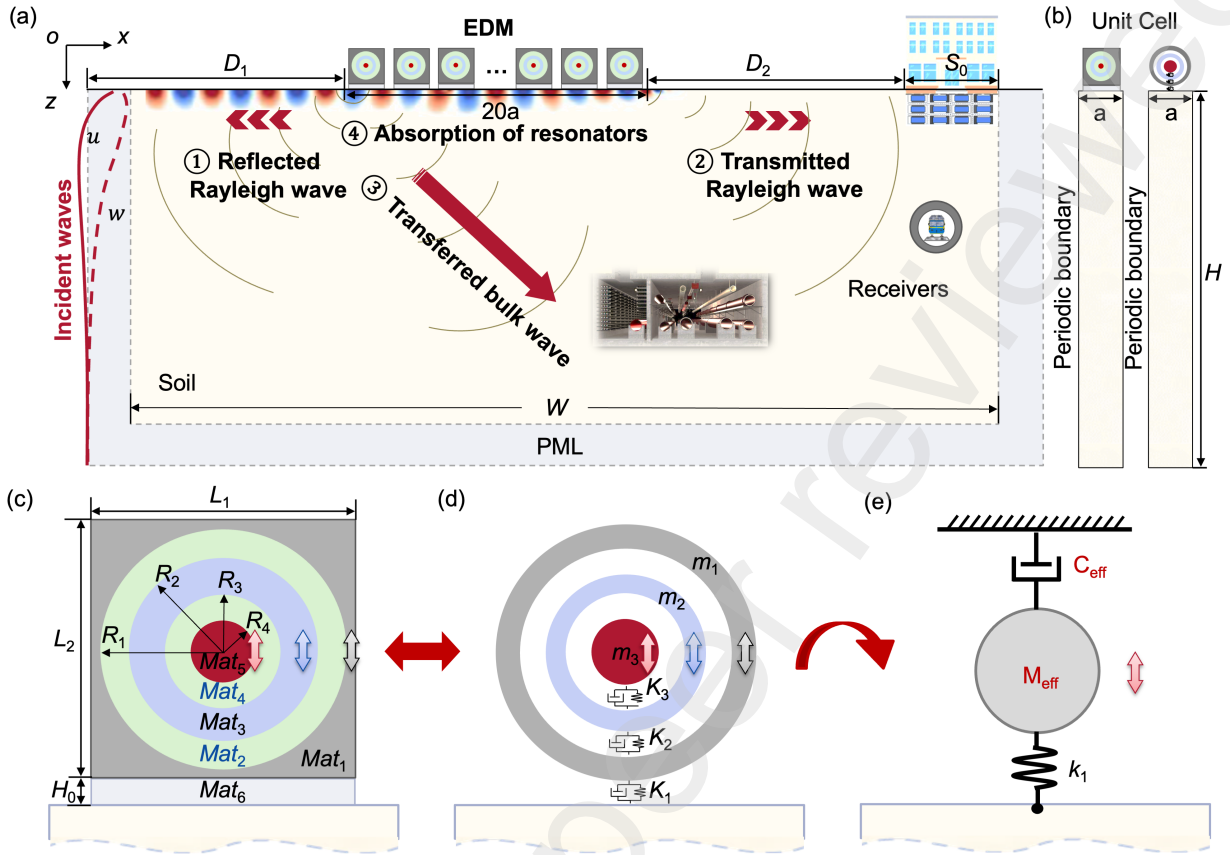


Figure 1: Schematic illustration of the EDMs for Rayleigh wave scattering mitigation. (a) Model depicting the four types of scattered energy from a 20-unit cell EDM, with the thickness of the PML being five times the wavelength, λ_R . (b) Unit cells of the EDM with physical resonators (left panel) and ideal resonators (right panel). (c) The geometry of physical resonators in the EDM. (d) The schematic diagram of ideal resonators. (e) The schematic diagram of the effective resonator model.

2.1. Theory of Rayleigh waves in elastic dissipative metasurface

A schematic diagram illustrating the use of EDMs for mitigating scattered waves is shown in Fig. 1(a) and the unit cells of EDMs on the substrate are shown in Fig. 1(b). The elastic half-space has the following parameters: Young's modulus $E = 4.60 \times 10^7$ Pa, the Poisson's ratio $\mu = 0.25$, and the mass density $\rho = 1800$ kg/m³. The width and height of the rectangular substrate are $W = 100a$ and $H = 20a$, respectively. Perfectly matched layers (PMLs) are applied to the bottom and side boundaries. An EDM consisting of 20 units is attached to the surface of the substrate, with distances D_1 and D_2 between the boundaries and the EDM both set to $40a$. The physical model of the local resonators, made of common engineering materials such as concrete, steel, lead, and rubber, is depicted in Fig. 1(c). The material parameters for the model in Fig. 1(c) are specified as listed in Table 1.

Due to the substantially lower elastic constants of the connecting layers (springs) relative to the rigid bodies (masses), the physical system can be effectively approximated as an ideal hierarchical mass-spring-damper model, as depicted in Fig. 1(d). The governing

101 equations for the three masses attached to the surface, expressed in the frequency domain,
 102 are formulated as follows:

$$m_1\omega^2 u_1(x) = K_1 [u_1(x) - w(x, 0)] + K_2 (u_1(x) - u_2(x)), \quad (1a)$$

$$m_2\omega^2 u_2(x) = K_2 [u_2(x) - u_1(x)] + K_3 [u_2(x) - u_3(x)], \quad (1b)$$

$$m_3\omega^2 u_3(x) = K_3 [u_3(x) - u_2(x)], \quad (1c)$$

105 where $u_1(x)$, $u_2(x)$ and $u_3(x)$ are the displacements of masses at position x , m_1 , m_2 and m_3
 106 are the masses of the resonators. The displacement of the substrate in the z -direction at
 107 position x when $z = 0$ is represented as $w(x, 0)$. The complex spring constants are defined as
 108 $K_j = k_j(1 + i\eta_j)$, $j = 1, 2, 3$, where k_1 , k_2 and k_3 are springs stiffnesses, and η_1 , η_2 and η_3 are
 109 the corresponding loss factors. The loss factor typically depends on the frequency and can
 110 be equivalently transformed into Rayleigh or viscous damping [60]. However, for simplicity,
 111 it is assumed to be a frequency-independent constant within the operating frequency range
 112 of 0 Hz to 26 Hz. This assumption is supported by experimental results for rubber [61],
 113 where the loss factor varies between 0 and 1.2.

114 The hierarchical mass-spring-damper model shown in Fig. 1(d) can be simplified to an
 115 effective mass-spring-damper model using effective theory, as illustrated in Fig. 1(e). The
 116 governing equation for the effective mass in Fig. 1(e) can be expressed as

$$m_{\text{eff}}\omega^2 u_1(x) = i c_{\text{eff}}\omega u_1(x) + K_1 [u_1(x) - w(x, 0)], \quad (2)$$

117 where m_{eff} is the effective mass and c_{eff} is the effective viscous coefficient, both of which are
 118 real numbers. To determine the effective mass and viscous coefficient, the variable vector
 119 $\mathbf{X} = [w(x, 0), u_1(x), u_2(x), u_3(x)]^T$ is decomposed into two subspaces: $\mathbf{X} = [\mathbf{X}_1, \mathbf{X}_2]^T$, where
 120 $\mathbf{X}_1 = [w(x, 0), u_1(x)]^T$ corresponds to the subspace of interest, and $\mathbf{X}_2 = [u_2(x), u_3(x)]^T$
 121 comprises the variables to be eliminated. Using this separation, Eq. (1) can be reformulated
 122 as a set of matrix equations:

$$\begin{bmatrix} \mathbf{H}_{11} & \mathbf{H}_{12} \\ \mathbf{H}_{21} & \mathbf{H}_{22} \end{bmatrix} \begin{bmatrix} \mathbf{X}_1 \\ \mathbf{X}_2 \end{bmatrix} = \begin{bmatrix} 0 \\ 0 \end{bmatrix}, \quad (3)$$

123 where

$$\begin{aligned} \mathbf{H}_{11} &= [-K_1 \quad -m_1\omega^2 + K_1 + K_2], \quad \mathbf{H}_{12} = [-K_2 \quad 0], \\ \mathbf{H}_{21} &= \begin{bmatrix} 0 & -K_2 \\ 0 & 0 \end{bmatrix}, \quad \mathbf{H}_{22} = \begin{bmatrix} -m_2\omega^2 + K_2 + K_3 & -K_3 \\ -K_3 & -m_3\omega^2 + K_3 \end{bmatrix}. \end{aligned} \quad (4)$$

124 Solving the second equation in Eq. (3), we obtain:

$$\mathbf{X}_2 = \mathbf{H}_{22}^{-1} \mathbf{H}_{21} \mathbf{X}_1. \quad (5)$$

125 Substituting this expression into the first equation of Eq. (3) results in:

$$\mathbf{H}_{\text{eff}} \mathbf{X}_1 = 0, \quad (6)$$

Table 1: Material parameters of the local resonators [47]

Material number	Mat1	Mat2	Mat3	Mat4	Mat5	Mat6
Material	Concrete	Rubber1	Steel	Rubber2	Lead	Rubber3
Lamé constants, λ_s (Pa)	8.33×10^9	2.00×10^5	1.00×10^{11}	2.00×10^7	2.96×10^9	4.00×10^5
Lamé constants, μ_s (Pa)	1.25×10^{10}	1.00×10^5	8.20×10^{10}	1.00×10^5	5.60×10^8	2.00×10^5
Density, ρ_s (kg/m ³)	2.80×10^3	1.30×10^3	7.89×10^3	1.00×10^3	1.13×10^4	1.00×10^3

126 where $\mathbf{H}_{\text{eff}} = \mathbf{H}_{11} - \mathbf{H}_{12}\mathbf{H}_{22}^{-1}\mathbf{H}_{21}$ is a 1 by 2 row vector, with its first element H_{eff}^1 equal to
127 $-K_1$. Consequently, Eq. (6) can be rewritten as

$$K_1 [u_1(x) - w(x, 0)] + (H_{\text{eff}}^2 - K_1) u_1(x) = 0, \quad (7)$$

128 where H_{eff}^2 is the second element of \mathbf{H}_{eff} . Since Eq. (7) is equivalent to Eq. (2), the effective
129 mass m_{eff} and the effective viscous coefficient c_{eff} in Eq. (2) can be determined by comparing
130 the coefficients of Eq. (2) and Eq. (7):

$$m_{\text{eff}} = -\frac{\text{Re}(H_{\text{eff}}^2 - K_1)}{\omega^2}, \quad (8a)$$

$$c_{\text{eff}} = \frac{\text{Im}(H_{\text{eff}}^2 - K_1)}{\omega}. \quad (8b)$$

131 Here, Re and Im represent the real and imaginary parts of a complex number, respectively.
132 This concludes the construction of the effective mass-spring-damper model derived
133 from the hierarchical mass-spring-damper system. Explicit expressions for calculating the
134 effective parameters in Eq. (8) are provided based on the material parameters defined in
135 Eq. (1). Although the derivation focuses on a hierarchical mass-spring-damper model with
136 three resonators, the theoretical framework can be generalized to hierarchical systems with
137 an arbitrary number of resonators.

138 On the surface of the substrate, the resonators apply point loads. Under the long-
139 wavelength approximation, these point loads can be treated as uniformly distributed loads.
140 As a result, the boundary conditions for normal stress σ_{zz} and shear stress σ_{xz} at the surface
141 $z = 0$, where the resonators are attached, can be expressed as

$$\sigma_{zz}(x, 0) = \frac{K_1}{a} [u_1(x) - w(x, 0)], \quad (9a)$$

$$\sigma_{xz}(x, 0) = 0. \quad (9b)$$

143 For the traveling wave, the wave solution of Rayleigh waves and resonators are expressed
144 as [52, 62]

$$u_1(x) = U_1 e^{i(kx - \omega t)}, \quad (10a)$$

$$w(x, z) = k (-qAe^{-kqz} + iBe^{-ksz}) e^{i(kx - \omega t)}, \quad (10b)$$

$$\sigma_{zz}(x, z) = \mu k^2 [2(rAe^{-kqz} - isBe^{-ksz})] e^{i(kx - \omega t)}, \quad (10c)$$

$$\sigma_{xz}(x, z) = -\mu k^2 [2iqAe^{-kqz} + rBe^{-ksz}] e^{i(kx - \omega t)}, \quad (10d)$$

149 where U_1, A, B are constants to be determined, ω is the angular frequency, k is the wavenumber,
 150 and the following relations hold:

$$q^2 - 1 + \left(\frac{c}{c_L} \right)^2 = 0, \quad s^2 - 1 + \left(\frac{c}{c_T} \right)^2 = 0, \quad r - 2 + \frac{c^2}{c_T^2} = 0, \quad (11)$$

151 where the wave speed $c = \omega/k$, the longitudinal wave speed is $c_L = \sqrt{\frac{\lambda+2\mu}{\rho}}$, and the shear
 152 wave speed is $c_T = \sqrt{\frac{\mu}{\rho}}$. Here, λ and μ are Lamé constants, and ρ is the density of the
 153 substrate. It is worth noting that the decay factors q and s must satisfy the following
 154 inequalities:

$$\operatorname{Re}(kq) > 0 \quad \text{and} \quad \operatorname{Re}(ks) > 0. \quad (12)$$

155 to ensure that the surface wave decays in the depth direction.

156 Substituting Eq. (10) and Eq. (11) into Eq. (9) yields the following system of linear
 157 homogeneous equations:

$$\begin{bmatrix} 2iq & r & 0 \\ \mu Lrk^2 + K_1 k q & -2i\mu s Lk^2 - iK_1 k & K_1 \\ K_1 k q & -iK_1 k & -m_{\text{eff}}\omega^2 + ic_{\text{eff}}\omega + K_1 \end{bmatrix} \begin{bmatrix} A \\ B \\ U_1 \end{bmatrix} = \begin{bmatrix} 0 \\ 0 \\ 0 \end{bmatrix}. \quad (13)$$

158 Eq. (13) can be compactly expressed in matrix form as $\mathcal{H}(\omega, r, q, s, k)\mathbf{U} = 0$. The
 159 dispersion relation $k(\omega)$ is determined by vanishing the determinant of the coefficient matrix:

$$\det(\mathcal{H}) = 0. \quad (14)$$

160 To derive the dispersion relation, the angular frequency ω is specified in advance, while
 161 other variables remain unknown. In a non-dissipative system, where all variables and poly-
 162 nomial equations are real, the system can be solved easily by eliminating variables. In this
 163 case, the wavenumber k is real, corresponding to propagating Rayleigh waves. Neverthe-
 164 less, in our dissipative system composed of masses and damped springs, all variables and
 165 polynomial equations are complex, complicating the process of solving these equations.

166 To address the complexity of solving Eqs. (11) and (14), a resultant-based elimina-
 167 tion theory from computational algebraic geometry is introduced to ensure precise and ef-
 168 ficient solutions [63]. The left-hand sides of Eqs. (14) and (11) are defined as polynomials
 169 $p_1(r, q, s, k)$, $p_2(q, k)$, $p_3(s, k)$, and $p_4(r, k)$, respectively. For a given ω , the resultant of p_1
 170 and p_2 with respect to q eliminates the variable q , yielding a new polynomial:

$$p_5(r, s, k) = \operatorname{Res}(p_1, p_2, q), \quad (15)$$

171 where Res is the resultant function, as defined in Appendix A. Similarly, taking the resultant
 172 of p_5 and p_3 with respect to s eliminates the variable s and gives a new polynomial:

$$p_6(r, k) = \operatorname{Res}(p_5, p_3, s). \quad (16)$$

173 Finally, taking the resultant of p_6 and p_4 with respect to r eliminates variable r and gives
 174 a new polynomial:

$$p_7(k) = \text{Res}(p_6, p_4, r). \quad (17)$$

175 The polynomial $p_7(k)$ is related solely to the wavenumber, enabling its roots to be deter-
 176 mined accurately using the “roots” function in MATLAB. To ensure physically meaningful
 177 results, redundant roots are discarded based on the inequalities in Eq. (12). For each valid
 178 root k , the corresponding q and s are determined using the resultant method similarly.
 179 Roots are retained only if the real parts of both q and s are positive; otherwise, they are
 180 discarded. By sweeping the frequency within a specified range and calculating the root k
 181 using the resultant method, the dispersion curves can be obtained completely and precisely.

182 2.2. Finite element method analysis

183 All simulations are performed by using the finite element method (FEM) in COMSOL
 184 Multiphysics. For the calculation of k - ω dispersion curves of the continuous model shown in
 185 the left panel of Fig. 1(b), we use the partial differential equations (PDEs) of elasticity based
 186 on Bloch’s theorem. These PDEs are solved using the “Coefficient Form PDE Interfaces.”
 187 For the calculation of k - ω dispersion curves of the discrete unit cell shown in the right
 188 panel of Fig. 1(b), the “Global ODEs and DAEs Interface” is also utilized to describe the
 189 effective mass-spring-damper system described in Eq. (2). For analyzing Rayleigh wave
 190 scattering depicted in Fig. 1(a), “Structural Mechanics Module” and “Global ODEs and
 191 DAEs Interface” in the frequency domain are used.

192 For a given frequency, the displacement distribution at the left boundary of PML is
 193 prescribed as

$$u = re^{-kqz} + 2sze^{-ksz}, \quad (18a)$$

$$w = iq(re^{-kqz} - 2e^{-ksz}), \quad (18b)$$

195 in the frequency domain to selectively excite a Rayleigh wave without generating any bulk
 196 waves, as shown in Fig. 1(a). Here, q , s , and k are determined by solving Eq. (14) and Eq.
 197 (11) for the given frequency in the absence of attached resonators.

198 To analyze the transmitted Rayleigh wave, the frequency response function (FRF) is
 199 defined as

$$\text{FRF} = \frac{20}{S_0} \log_{10} \left(\int_{S_0} \frac{|w|}{|w_0|} dx \right), \quad (19)$$

200 where S_0 is the length of the surface receiver in Fig. 1(a), w (w_0) is the displacement
 201 component along the z -direction calculated from the model with (without) the EDM.

202 3. Mitigation of Rayleigh wave scatterings by EDMs with single local resonance

203 In this section, we start with the simplest model, employing an EDM with single local
 204 resonators to attenuate transmitted Rayleigh waves. The resonators have a stiffness of
 205 $k_1 = 1.9 \times 10^7$ N/m and a mass of $m_1 = 2000$ kg. We use both dispersion relations and FRF
 206 to characterize wave transmission. Additionally, an energy analysis provides deeper insights

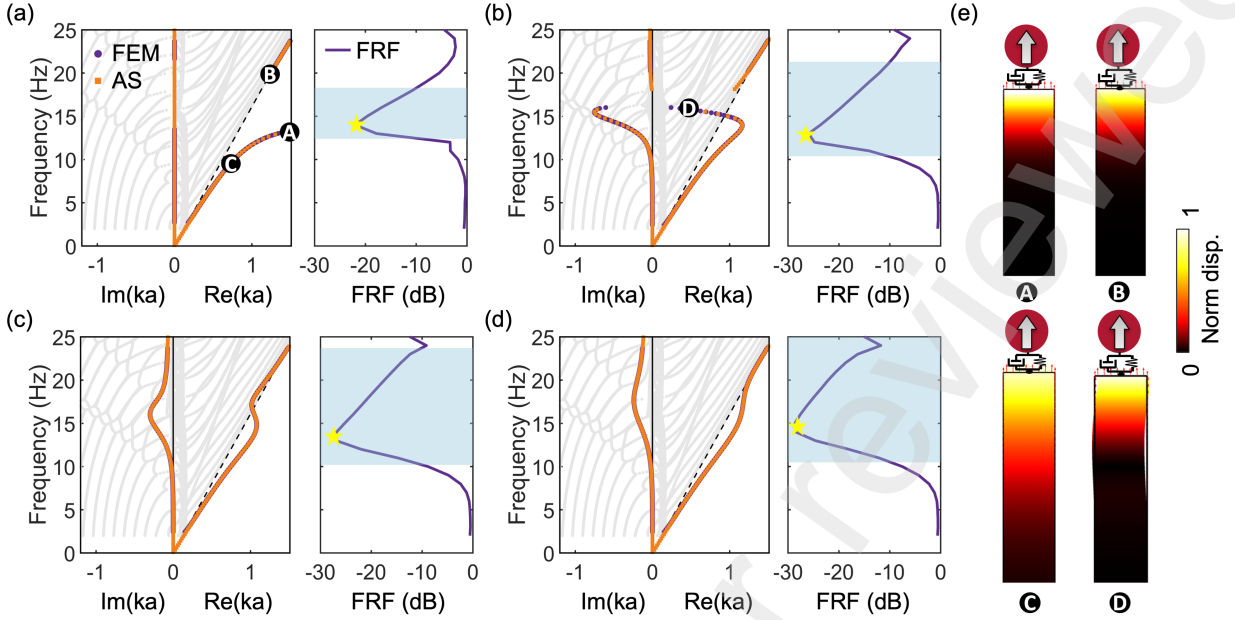


Figure 2: Complex dispersion curve diagrams, transmission FRF, and mode. (a)-(d) Dispersion diagrams and FRF for the loss factor $\eta = 0, 0.3, 0.6$, and 0.9 , respectively. In the left panels of (a)-(d), the gray curves correspond to bulk waves from FEM unit cell analysis, whereas the purple (FEM analysis) and orange curves (analytical solution (AS) described in Section 2) represent the complex dispersion curves of Rayleigh waves. In the right panels of (a)-(d), the light blue region represents the stopband with < -10 dB transmission. (e) Corresponding mode shapes of the four eigenmodes A, B, C, and D highlighted in panels (a) and (b).

207 into the complex interactions between Rayleigh waves and the EDM. In this analysis, we
208 decompose the bulk waves into P and SV waves and examine wave mode conversion in the
209 bulk using a 2D Fourier transform (FT). The damping effect on Rayleigh wave scattering is
210 considered throughout this section.

211 3.1. Dispersion analysis and transmitted Rayleigh waves mitigation

212 First, we calculate the dispersion curves presented in the left panels of Figs. 2(a-d).
213 The dispersion curves of the Rayleigh wave, obtained from finite element method (FEM)
214 analysis (purple) and analytical approach from Eq. (14) (orange), are in excellent agreement,
215 confirming the accuracy of the analytical model. In this case, we have $k_2 = k_3 = m_2 = m_3 =$
216 $\eta_2 = \eta_3 = 0$ and define η_1 as η .

217 In the absence of damping ($\eta = 0$), the dispersion bands of Rayleigh waves are all real,
218 and a bandgap emerges due to the local resonance. The mode shapes of the highlighted
219 modes A, B, and C are shown in Fig. 2(e), which demonstrate an exponentially decaying field
220 intensity in the depth direction. When damping is presented ($\eta \neq 0$), the imaginary parts
221 of dispersion curves are non-zero, while the real parts of dispersion curves bend for small
222 damping or connect to higher frequency bands for larger ones. The imaginary dispersion
223 indicates a decaying Rayleigh wave, where the decay factor is proportional to the imaginary
224 wavenumber. It is noteworthy that even though the Rayleigh band warps into the sound

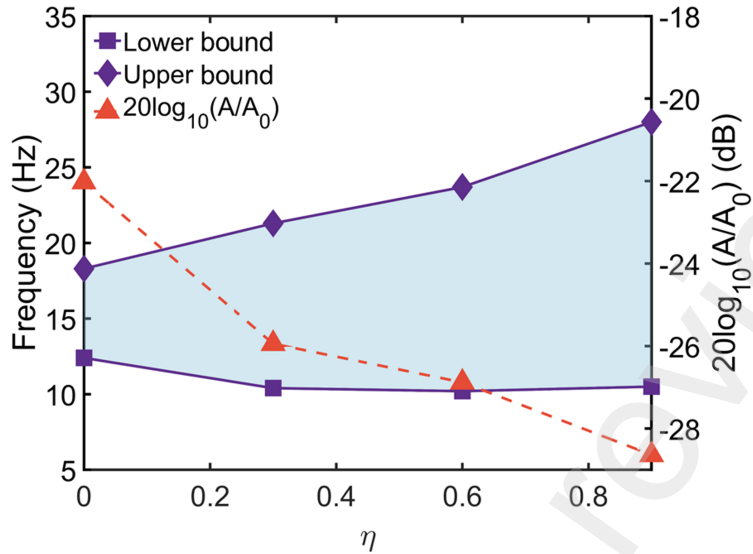


Figure 3: The bandwidth at -10 dB (purple region) and minimum FRF (orange dashed line) in the function of loss factor η . The data are obtained from the right panels of Figs. 2(a-d).

cone, it still belongs to a Rayleigh wave mode rather than a bulk mode, as illustrated in Fig. 2(e) mode D.

To fully capture the transmission property of the EDM, we show the FRF results in the right panels of Figs. 2(a-d). Here, we define the effective stopband as the light blue region where the FRF is less than -10 dB. The effect of damping on the stopband range and the minimum FRF is shown in Fig. 3. We can observe that a higher loss factor simultaneously enhances the bandwidth of the stopband and decreases the minimum transmission, leading to significantly suppressed transmission.

3.2. Energy analysis of Rayleigh wave scatterings by EDMs

The energy of the incident Rayleigh wave is transformed into four distinct parts by EDMs. To quantitatively characterize the energy transformation, we employ an energy analysis method based on the concept of frequency-dependent elastic energy flux \mathbf{I} , or elastic Poynting's vector, defined as [63]

$$\mathbf{I} = -\frac{1}{2}\text{Re}(\boldsymbol{\sigma}^* \cdot \mathbf{v}), \quad (20)$$

where $\boldsymbol{\sigma}$ is the stress tensor, $(\cdot)^*$ is the complex conjugate operator, \mathbf{v} is the velocity vector. The energy of reflected Rayleigh wave E_r , transmitted Rayleigh wave E_t , scattered bulk wave E_b , and dissipation from resonators E_l are defined as the following:

$$E_r = E_i + \int_{S_1} \mathbf{I} \cdot \mathbf{n} dS, \quad (21a)$$

$$E_t = \int_{S_2} \mathbf{I} \cdot \mathbf{n} dS, \quad (21b)$$

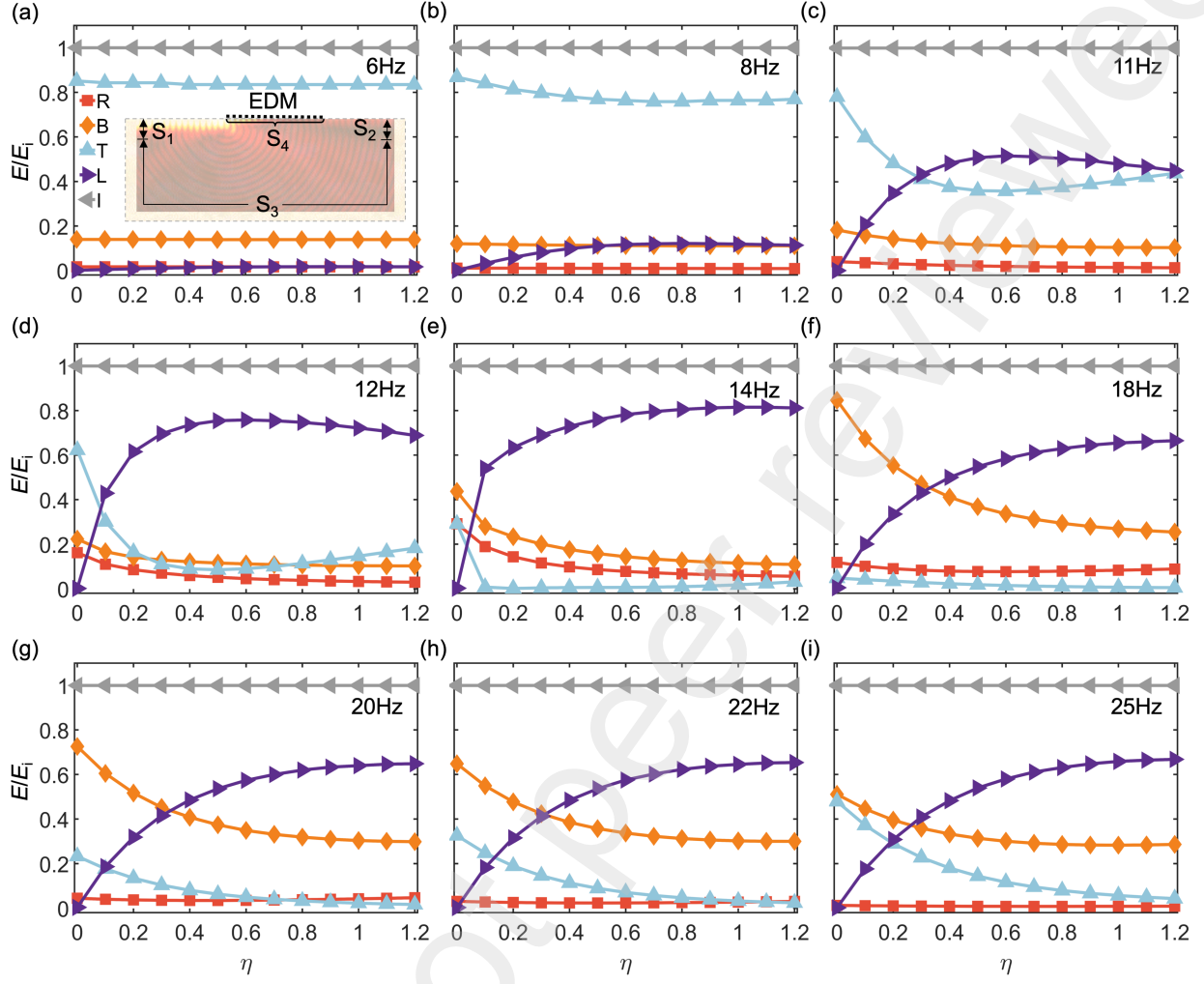


Figure 4: The energy (E) normalized by the incident energy is categorized as reflected Rayleigh wave (R), transferred bulk wave (B), transmitted Rayleigh wave (T), resonator absorption (L), and incident wave (I) with respect to different loss factors and different frequencies. S_1 , S_2 , S_3 , and S_4 are the regions for calculating the energy of reflected Rayleigh wave, transmitted Rayleigh wave, bulk waves, and absorption by the EDM.

242

$$E_b = \int_{S_3} \mathbf{I} \cdot \mathbf{n} dS, \quad (21c)$$

$$E_l = \frac{1}{2} \int_{S_4} \text{Re}(\boldsymbol{\sigma}^* : i\omega\boldsymbol{\epsilon}) dS, \quad (21d)$$

243 where \mathbf{n} is the unit vector pointing in the direction of the outward normal, $\boldsymbol{\epsilon}$ is the strain
 244 tensor, and the energy of incident Rayleigh wave is $E_i = |\int_{S_1} \mathbf{I}_i \cdot \mathbf{n} dS|$. Here, \mathbf{I}_i is the energy
 245 flux of the incident Rayleigh wave which can be calculated from the homogeneous elastic
 246 medium in the absence of EDMs. Additionally, the definition of surfaces S_1 , S_2 , S_3 , and S_4
 247 can be found in the inset of Fig. 4(a).

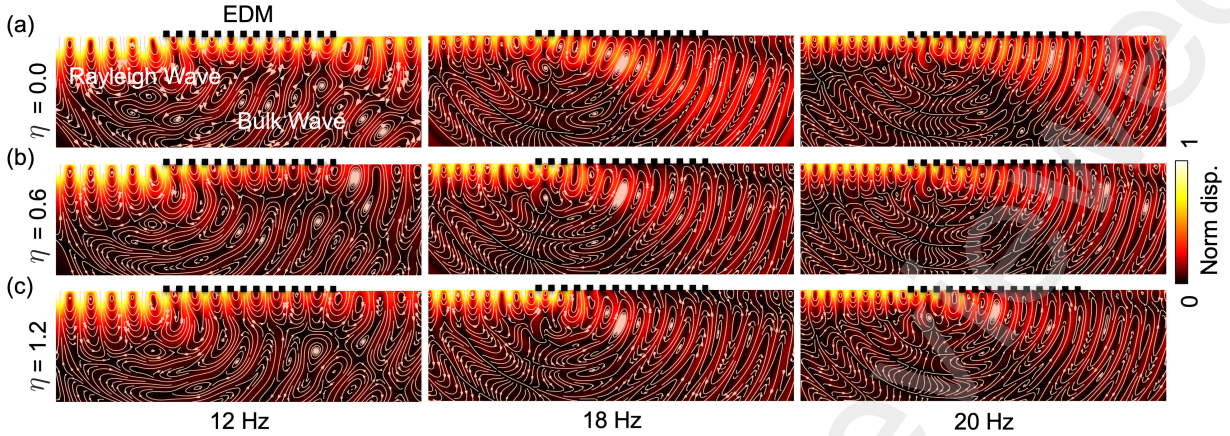


Figure 5: The wave scattering field of an incident Rayleigh wave at frequencies 12 Hz, 18 Hz, and 20 Hz, and loss factors (a) $\eta = 0.0$, (b) $\eta = 0.6$, and (c) $\eta = 1.2$.

According to Poynting's theorem, the energy of an incident Rayleigh wave is equal to the summation of the energy of the transmitted Rayleigh wave, reflected Rayleigh wave, scattered bulk wave, and absorption by resonators. This can be expressed as:

$$E_i = E_r + E_t + E_b + E_l. \quad (22)$$

In Fig. 4, we illustrate how each energy component is influenced by the loss factor and the frequency near the stopband (6 Hz to 25 Hz). Incident energy is normalized for convenience. At frequencies below 8 Hz, Rayleigh waves exhibit a long penetration depth, leading to minimal energy confinement at the surface and limited interaction with the resonators. Consequently, the majority of energy (85%) is transmitted, while the remaining energy (15%) is scattered into bulk waves at the left interface of the EDM. These energy ratios are largely independent of the loss factor, as demonstrated in Fig. 4(b). As the frequency reaches 8 Hz, the penetration depth of Rayleigh waves decreases, increasing interaction with the resonators. Incident wave energy begins to dissipate through the resonators. As the frequency approaches the resonant frequency (13.5 Hz), the coupling between Rayleigh waves and local resonance becomes more pronounced, and energy flows in all four directions, as shown in Figs. 4(c-d). At 12 Hz, the energy of the Rayleigh wave dissipates significantly as η increases, as shown in the left panels in Fig. 5. It is noteworthy that the decay factor of the Rayleigh wave does not vary monotonically with the loss factor, as demonstrated in Fig. 2. As a result, we can observe a decrease in transmitted wave energy followed by an increase in Fig. 4(d).

For EDM operating within the bandgap (13.5 to 19 Hz) with $\eta = 0$, the energy of the reflected wave and bulk waves dominates, with minimal transmitted wave energy, as the Rayleigh wave cannot propagate within the bandgap, as shown in Figs. 4(e-f). As η increases, the loss factor reduces resonance and introduces the horizontally decaying Rayleigh waves, causing an increase in dissipated energy while other energies decrease, as observed in the middle panels of Figs. 5(a-c). When the frequency exceeds the upper bound of the

bandgap, the impact of local resonance diminishes, leading to a decrease in bulk wave energy and an increase in transmitted wave energy. In this region, the loss factor further diminishes bulk waves and Rayleigh wave energies in the EDM, resulting in decreased energies of both bulk waves and transmitted waves as η increases, as depicted in the right panels of Figs. 5(a-c). Figure 4 illustrates that without damping, local resonance significantly reduces transmitted wave energy but introduces other scattered waves in the bandgap region (13.5 to 19 Hz). The damping in the local resonators greatly reduces these scattered waves near the bandgap region (12 to 19 Hz). If the damping is substantial, the transmitted wave can also be eliminated above the bandgap, though bulk waves cannot be entirely mitigated.

We can conclude that EDM with single local resonances effectively attenuates Rayleigh waves with the correct combination of frequency, loss factor, and energy distribution. While the effect is weak at extremely low frequencies, a slight increase in the loss factor at mid-frequencies significantly enhances energy dissipation through resonator absorption. At high frequencies, the effect stabilizes, but excessive damping can reduce energy conversion efficiency. The EDM effectively converts Rayleigh wave energy into other forms, primarily via bulk wave conversion and resonator absorption. This conversion mechanism is influenced by both the frequency of the incident waves and the damping properties of the EDM.

3.3. Bulk waves decomposition

In the current system, bulk waves consist of both P and SV waves. We decompose bulk waves into P and SV waves and discuss each of their propagation. P and SV waves are separated by taking the divergence and curl of the displacement field, respectively. The primary propagation direction is determined by performing a 2D FT on the divergence and curl, as illustrated in Figs. 6(a,d) for a frequency of 12 Hz and $\eta = 0.3$. By integrating the amplitude in the 2D reciprocal space along the radial direction, we obtain polar diagrams for different frequencies and loss factors, depicted in Figs. 6(b,c,e,f). In these figures, the magnitude of P waves is significantly smaller than that of SV waves, indicating that SV waves dominate the bulk waves scattered by the EDM (Figs. 6(a,d)). In Figs. 6(b-c) and 6(e-f), P waves are primarily propagating along z direction, while SV waves have a larger component in x direction. The magnitude of P and SV waves decreases with increasing damping near the resonance frequency, indicating that damping effectively reduces these waves. These analyses reveal that Rayleigh-to-bulk wave conversion primarily results in z -propagating P waves and predominantly x -propagating SV waves. The result can be helpful in determining underground wave types, providing insights into the design of underground devices. Furthermore, the loss factor significantly reduces bulk waves near the resonance frequency, underscoring its importance in wave mitigation strategies.

4. Rayleigh wave mitigation by multi-resonant EDMs

4.1. Microstructure design and dispersion analysis

As previously discussed, EDMs are highly effective in attenuating transmitted Rayleigh waves near their resonance frequencies. When equipped with multiple resonators, EDMs can mitigate Rayleigh waves near these specific resonance frequencies but cannot effectively

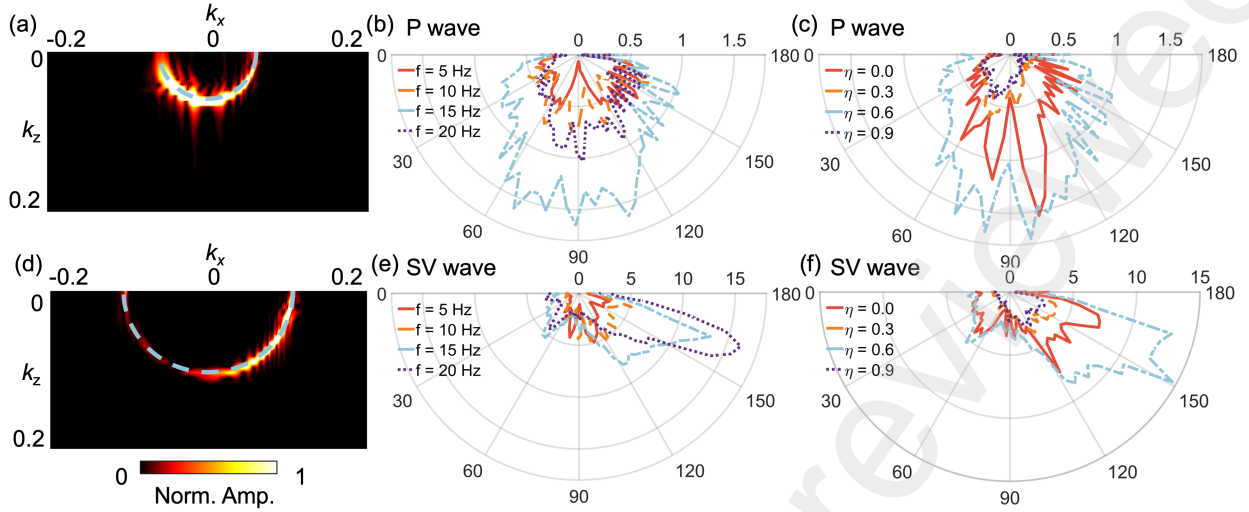


Figure 6: Angle analysis of transferred P and SV waves. (a) The 2D FT of the divergence of the displacement field (P wave) at a frequency of 12 Hz and a loss factor of 0.3. (b) The polar diagram of the transferred P wave with a loss factor of 0 across different frequencies. (c) The polar diagram of the transferred P wave at 12 Hz for varying loss factors. (d) The 2D FT of the curl of the displacement field (SV wave) at a frequency of 12 Hz and a loss factor of 0.3. (e) The polar diagram of the transferred SV wave with a loss factor of 0 across different frequencies. (f) The polar diagram of the transferred SV wave at 12 Hz for varying loss factors.

block the Rayleigh waves far from these frequencies. However, damping can broaden the resonance peaks, resulting in broadband attenuation of transmitted Rayleigh waves. In this section, we examine EDMs with three dissipative resonators. The mass-spring parameters, listed in Table 2, and the geometric parameters of the physical model, illustrated in Fig. 1(c), are then inversely determined from numerical tests in Fig. 7.

The mass m_3 and its density are known, allowing the radius R_1 to be determined from its volume. Subsequently, for a given R_3 , a displacement is applied to the mass m_3 while the mass m_2 remains fixed, and the resulting reaction force is extracted in COMSOL. The stiffness k_3 is then calculated as the ratio of the reaction force to the prescribed displacement. By varying the radius R_3 , the relationship between k_3 and R_3 is established and plotted in Fig. 7(a). For a specific k_3 , the corresponding geometric parameter R_3 is determined using a graphical method. Next, R_2 is determined from its volume, and the geometric parameter R_3 is identified using the graphical method shown in Fig. 7(b). Here, the stiffness k_2 is calculated by fixing the mass m_1 and applying a prescribed displacement to m_2 for a given R_1 . Finally, R_1 is determined from its volume, and the geometric parameter H_0 is identified using the graphical method shown in Fig. 7(c). In this case, the stiffness k_1 is calculated by fixing the substrate and applying a prescribed displacement to m_1 for a given H_0 .

We then discuss the dispersion curves, mode shapes, and the effect of damping on the discrete and continuous models. The dispersion curves of the analytical model (orange) and the continuous model (purple) are illustrated in Fig. 8(a), with corresponding mode shapes shown in Figs. 8(b) and 8(c), respectively. As shown in Fig. 8(a), within the frequency range

Table 2: Parameters of local resonators.

Mass of resonator	Value (kg)	Stiffness of resonator	Value (N/m)
m_1	989	k_1	3.98×10^7
m_2	1128	k_2	6.58×10^6
m_3	1890	k_3	4.17×10^6

Table 3: Geometrical parameters of the local resonators.

Parameters	a	L_1	L_2	H_0	R_1	R_2	R_3	R_4
Length (m)	2.00	1.00	1.00	0.05	0.475	0.375	0.325	0.225

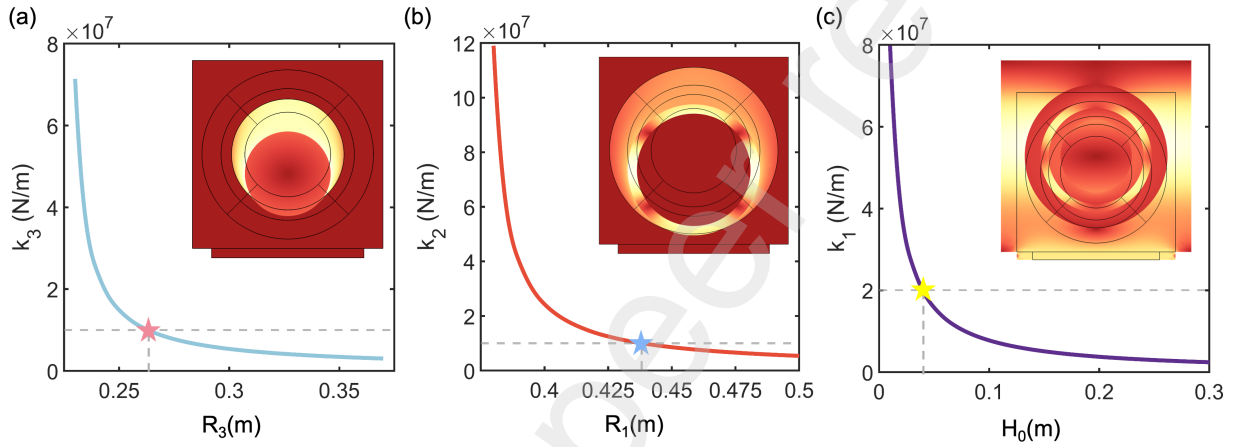


Figure 7: Stiffness of EDMs with three resonators (k_1 , k_2 , and k_3) under numerical tests and the optimal design corresponding to the actual structural geometry: (a) the intermediate resonator radius R_3 , (b) the outermost resonator radius R_1 , and (c) the element side length H_0 .

of interest, two bandgaps are generated by the local resonators m_2 and m_3 . In contrast, the resonance frequency of m_1 is well above 25 Hz, placing the bandgap associated with this resonator significantly outside the frequency range of interest.

For different combinations of loss factors η_2 and η_3 (0.3, 0.6, and 0.9, respectively), Figs. 8(d-f) show that loss factor η_2 affects the resonance at higher frequencies, whereas loss factor η_3 affects the resonance at lower frequencies. Increasing the loss factors η_2 or η_3 significantly broadens the peaks in imaginary parts, and simultaneously increasing both factors links those two imaginary peaks, enabling broadband attenuation of Rayleigh waves in EDMs.

4.2. Effective model

Now, we turn to describe the behavior of the effective mass m_{eff} and effective damping c_{eff} , which can be utilized to quickly predict the dispersion curves and the decaying behavior of Rayleigh waves in EDMs. In Fig. 9, the resonance of two inner resonators induces two sharp peaks and two sharp valleys in the effective mass when damping is small. At these valleys, the effective mass becomes negative. Negative mass regions are not perfectly aligned with the bandgap regions in the dispersion curves but are very close due to the influence

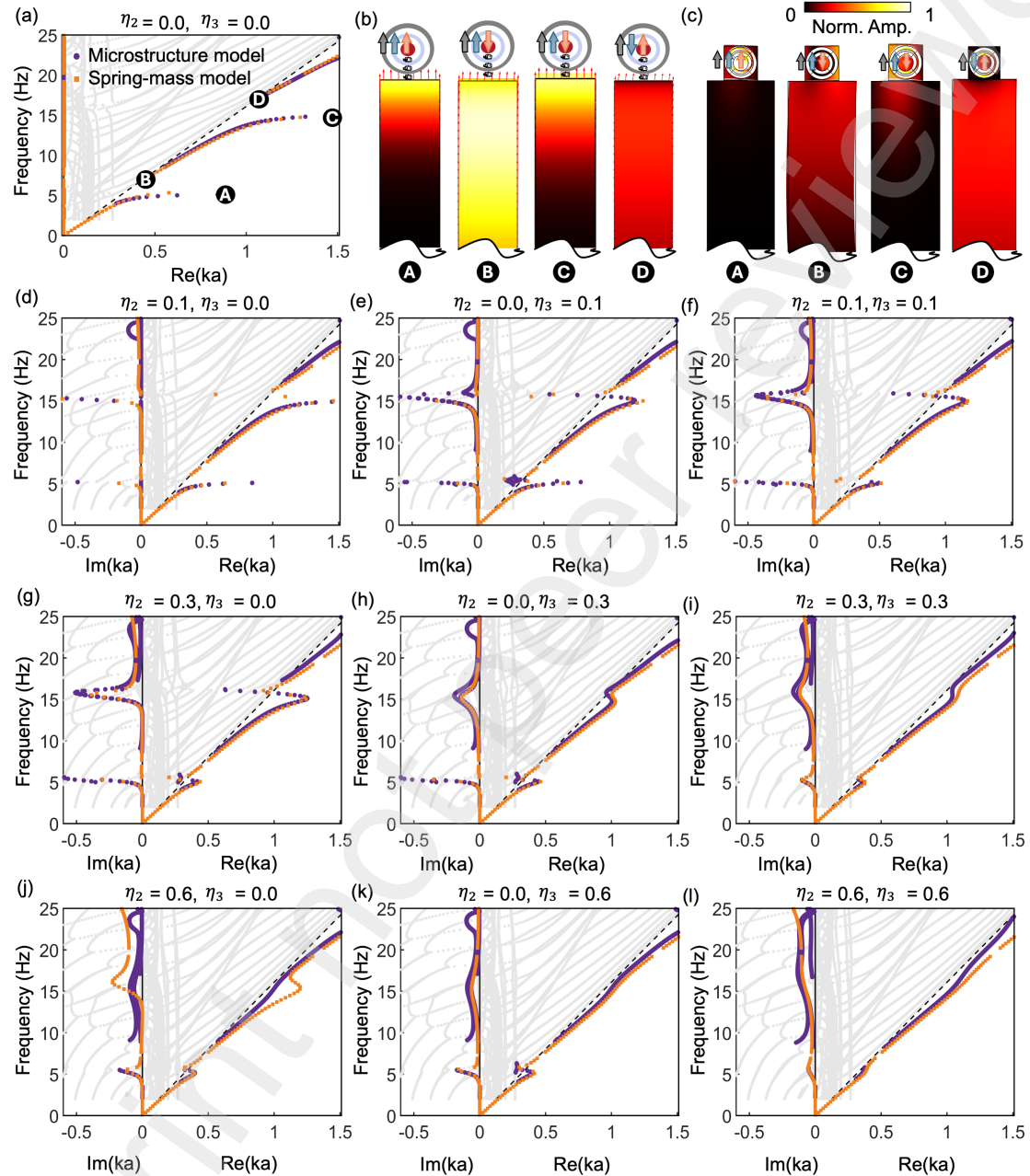


Figure 8: (a) Dispersion curves of the EDM with an array of triple damped resonators for $\eta_2 = \eta_3 = 0$. The gray curves are dispersion curves of bulk waves from unit cell analysis, whereas purple curves (continuous model analysis) and orange curves (analytical method described in section 2) represent dispersion curves of Rayleigh waves. (b-c) The mode shapes. (d-l) Dispersion curves of EDMs with an array of triple-damped resonators for different combinations of η_2 and η_3 .

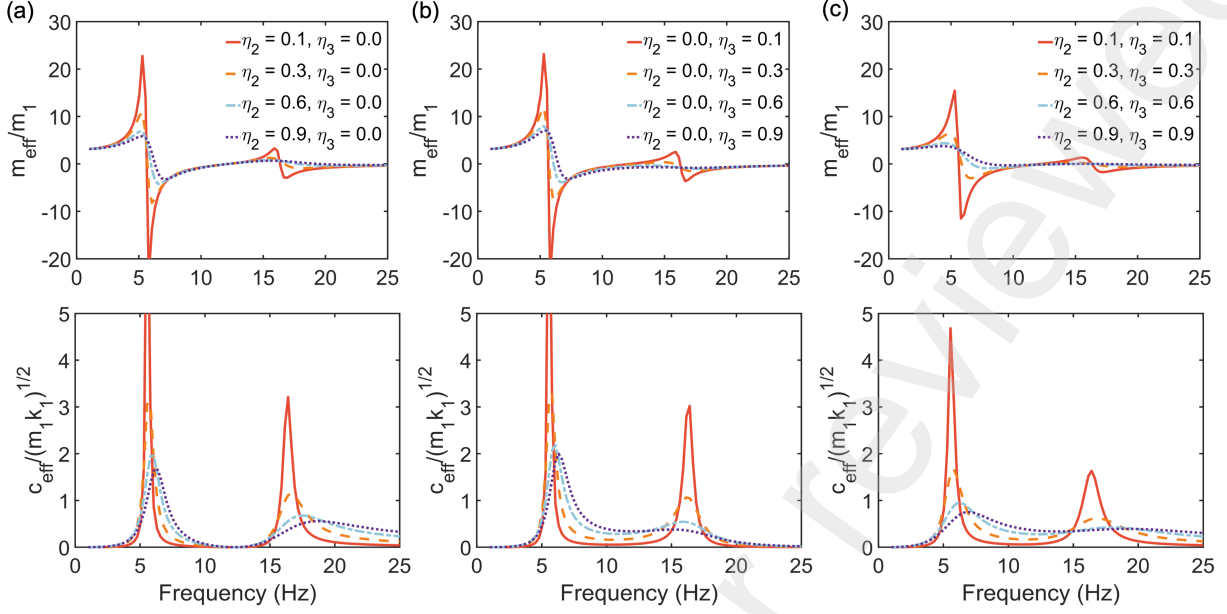


Figure 9: Effective mass and effective metadamping coefficient of EDM lattice system with three resonators with different loss factors: (a) $\eta_2 = 0.1, 0.3, 0.6, 0.9$; $\eta_3 = 0.0$, (b) $\eta_3 = 0.1, 0.3, 0.6, 0.9$; $\eta_2 = 0.0$, and (c) $\eta_2 = \eta_3 = 0.1, 0.3, 0.6, 0.9$.

of bulk waves. Consequently, the bandgaps in the dispersion curves can be approximately predicted by identifying the negative mass region under low damping conditions. As damping increases, it broadens the width and reduces the height of c_{eff} peaks, as shown in Fig. 9. The width of both peaks increases with an increment in either η_2 or η_3 , as depicted in Figs. 9(a-b). Notably, η_2 significantly broadens the higher frequency peak while only slightly affecting the lower frequency one. On the other hand, η_3 predominantly contributes to the broadening of the lower frequency peak. When both η_2 and η_3 are large, the c_{eff} peaks merge, forming a continuous response over a broad frequency range (5 to 25 Hz). When compared with Fig. 8, the influence of c_{eff} mirrors its effect on the imaginary component of the dispersion curves, particularly when damping is significant. Therefore, effective damping c_{eff} can quickly predict the imaginary part of the dispersion curves and the decaying behavior of Rayleigh waves in EDMs.

4.3. Transmission analysis in the frequency domain

The imaginary component of the dispersion curves governs the decaying factor of Rayleigh waves within the EDMs. If the Rayleigh waves decay rapidly, the transmitted wave is minimal. However, this factor alone is insufficient to quantitatively predict the transmitted wave, as it does not account for the presence of scattered waves. Therefore, we analyze the FRF in the frequency domain to obtain the effect of damping on transmitted waves. In Fig. 10(a), the first stopband widens as loss factor η_2 increases, but the attenuation amplitude initially increases before subsequently decreasing. In Fig. 10(b), a high-frequency stopband rapidly forms, significantly enhancing wave attenuation, though low-frequency attenuation

370 diminishes with increasing η_3 . When η_2 and η_3 increase simultaneously, all bands merge to
371 form a complete stopband (see Fig. 10(c)).

372 Figure 10(d-g) depicts the scattering fields of an incident Rayleigh wave at various fre-
373 quencies (6 Hz, 15 Hz, and 23 Hz) for different EDM loss factors. It can be observed that
374 after passing through the non-dissipative metasurface ($\eta_2 = \eta_3 = 0$), the Rayleigh wave
375 shows a significant reduction in transmission at 6 Hz and almost zero transmission at 15
376 Hz, confirming the effectiveness of the EDM in regulating low-frequency Rayleigh waves at
377 sub-wavelength scales (see Fig. 10(d)). With EDMs ($\eta_2, \eta_3 > 0$), Rayleigh waves can still
378 propagate through at 6 Hz, but large loss factors significantly reduce transmission (see the
379 left panels of Figs. 10(e-g)). Unlike a non-dissipative metasurface, which directly scatters
380 off the incident Rayleigh wave at 15 Hz, the EDM interacts with the incident wave and dis-
381 sipates the energy. This phenomenon is clearly observed in the middle panels of Fig. 10(g).
382 However, higher damping results in less energy dissipation within the EDM and greater
383 conversion of Rayleigh waves to bulk waves at 23 Hz, thereby increasing transmitted energy
384 (see the right panels of Figs. 10(e-g)).

385 This FRF analysis aligns with the equivalent model predictions in Fig. 9, demonstrating
386 the EDM's effectiveness at sub-wavelength scales. These findings indicate that η_2 primarily
387 affects the low-frequency stopband, while η_3 primarily affects the high-frequency stopband.
388 Their combined effect achieves significant wave energy absorption and stopband formation
389 over a broad frequency range, ensuring the broadband absorption required for low-frequency
390 vibration isolation.

391 5. Rayleigh waves in media with slowly space-varying EDMs and their applica- 392 tions

393 5.1. Rayleigh waves in slowly space-varying EDMs

394 In previous sections, we developed a theoretical framework for describing Rayleigh waves
395 by incorporating a uniform EDM composed of local resonators. However, a uniform arrange-
396 ment often leads to significant wave reflection and bulk wave scattering, especially near the
397 resonant frequency. These reflected Rayleigh waves and scattered bulk waves may give rise
398 to unexpected issues in engineering applications, such as in surface acoustic wave devices.

399 To address this issue, we propose a slowly space-varying EDM that acts as a perfect
400 absorber for broadband Rayleigh waves, functioning as a "rainbow surface absorber" (see
401 Fig. 11(a)). In this section, we first conduct a local unit cell analysis and explain its
402 application for predicting wave propagation in the slowly space-varying system [55, 54, 57].
403 We then verify the wave behavior predicted from this analysis in both the frequency domain
404 and time domain. Finally, we design a boundary absorber and a Rayleigh wave amplitude
405 modulator based on these results. Here, single-resonant EDMs are used for verification, as
406 shown in Fig. 1(a), but the paradigm is the same as that for multi-resonant EDMs.

407 In Fig. 11(a), we present a schematic diagram illustrating wave propagation in a slowly
408 space-varying EDM on a semi-infinite substrate. The EDM comprises 100 resonators to
409 guarantee adiabatic conditions, which will be validated a posteriori. The side width of
410 resonators increases from 0.2 m to 0.7 m as x varies from 0 to $W = 200$ a, as illustrated in Fig.

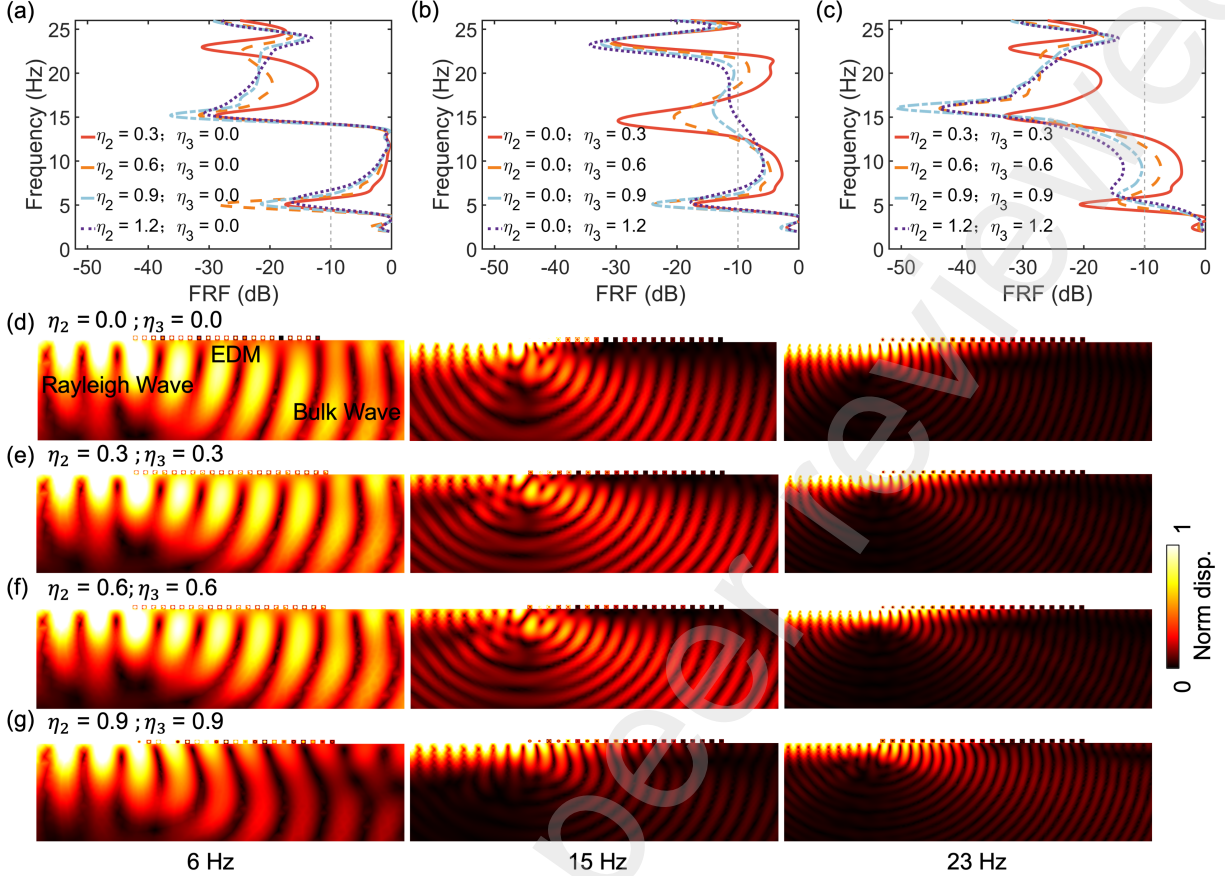


Figure 10: The EDM wave scattering field of the actual structure with three resonators cavity and the FRF under different loss factors: (a) $\eta_2 = 0.3, 0.6, 0.9, 1.2$; (b) $\eta_3 = 0.3, 0.6, 0.9, 1.2$; and (c) $\eta_2 = \eta_3 = 0.3, 0.6, 0.9, 1.2$. The wave scattering field of an incident Rayleigh wave at frequencies of 6 Hz, 15 Hz, and 23 Hz, with loss factors (d) $\eta_2 = \eta_3 = 0.0$, (e) $\eta_2 = \eta_3 = 0.3$, (f) $\eta_2 = \eta_3 = 0.6$, and (g) $\eta_2 = \eta_3 = 0.9$. The color scale indicates the elastic strain energy density level.

411 11(b). Under the adiabatic conditions, the Rayleigh wave propagates without scattering, as
 412 shown in Fig. 11(a). However, along the x axis, the wavelength $\Lambda = 2\pi/k$ is no longer a
 413 constant. The wavenumber $k(\phi)$ becomes a function that changes continuously from left to
 414 right, and $k(\phi)$ at normalized position $\phi = x/W$ can be determined by performing the local
 415 unit cell analysis.

416 For the local unit cell analysis, we first obtain the dispersion surface, a function of $k(f, \phi)$,
 417 of the Rayleigh wave by sweeping ϕ and f . The real and imaginary parts of this function are
 418 shown in Figs. 11(c) and 11(e), respectively. We then plot frequency planes at 10 Hz and
 419 18 Hz (purple for 10 Hz and orange for 18 Hz). The intersection of these frequency planes
 420 and the dispersion surfaces provides the wavenumber function $k(\phi)$, as shown in Figs. 11(d)
 421 and 11(f). The real part of wavenumber $\text{Re}(k(\phi))$ in Fig. 11(d) and the imaginary part
 422 of wavenumber $\text{Im}(k(\phi))$ in Fig. 11(f) determine the local wavelength and decay factor at
 423 position x in Fig. 11(a). After obtaining the wavenumber function $k(\phi)$, the evolution of

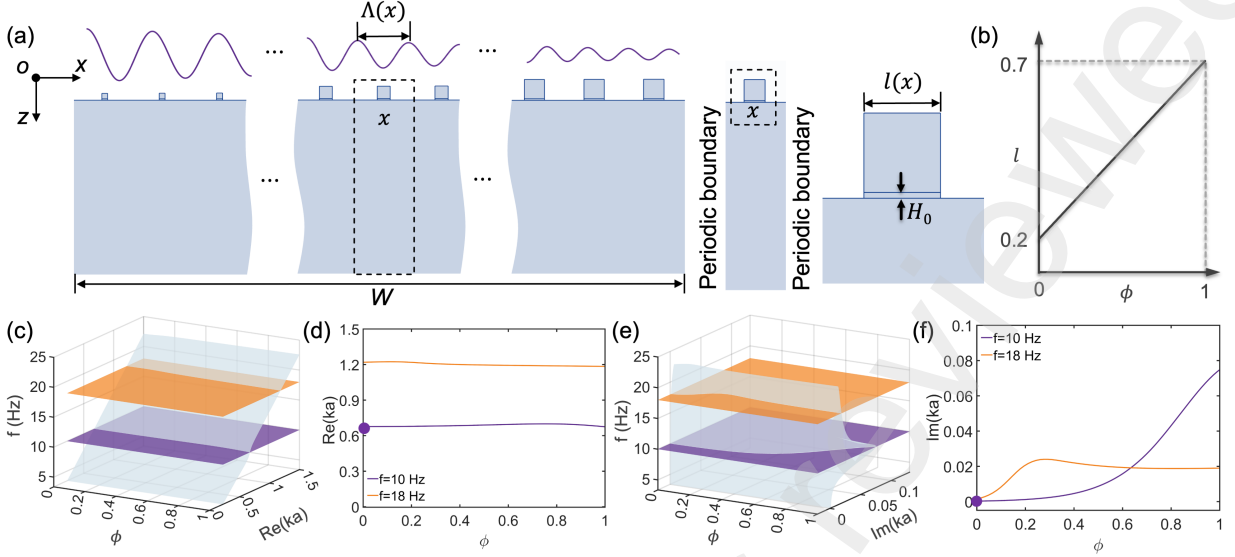


Figure 11: Principle of the adiabatic evolution of Rayleigh waves within a slowly space-varying damping system. (a) Schematic diagram illustrating surface wave propagation in a slowly space-varying EDM. (b) Variation of the side length of the resonator l as a function of the normalized spatial coordinate $\phi = x/W$. (c) The real part of the dispersion surface for Rayleigh waves overlaid with frequency planes corresponding to excitation frequencies of 10 Hz (purple) and 18 Hz (orange). (d) Curves representing the intersections of the frequency planes and the real part of the dispersion surface are depicted in (c). (e) The imaginary part of the dispersion surface for Rayleigh waves, with frequency planes at excitation frequencies of 10 Hz (purple) and 18 Hz (orange). (f) Curves showing the intersections of the frequency planes and the imaginary part of the dispersion surface described in (e).

the Rayleigh wave can be predicted by the adiabatic theorem. If the initial eigenvalue, the wavenumber k of the Rayleigh wave, is excited with a frequency of 10 Hz (see the purple dot in Figs. 11(d) and 11(f) with $\phi = 0$), the Rayleigh wave will propagate from left to right without mode conversion. The local wavenumber and decay factor will follow the purple curves in Figs. 11(d) and 11(f).

5.2. Numerical verifications of Rayleigh waves in slowly space-varying EDMs

Now we turn to the discussion of Rayleigh wave behavior in the frequency domain. The frequency domain response of the structure depicted in Fig. 11(a) at 10 Hz (top panel) and 18 Hz (bottom panel) is presented in Fig. 12(a). We observe that the Rayleigh wave decays along the x axis, with no observable bulk wave, reflected wave, or transmitted wave, thereby qualitatively verifying that the adiabatic condition is satisfied. The resulting Rayleigh wave will propagate undisturbed until being fully dissipated by EDMs.

To quantitatively analyze the evolution of the Rayleigh wave, the real part of displacement field w at $z = 3$ m is plotted in Figs. 12(b) and 12(d) for excitation frequencies of 10 Hz and 18 Hz, respectively. To extract the local wavenumber at various positions, we perform a wavelet transformation on the data presented in Figs. 12(b) and 12(d), which are displayed in Figs. 12(c) and 12(e). The wavenumber remains almost invariant along the x axis, with the normalized central wavenumber close to 0.7 at 10 Hz and 1.2 at 18

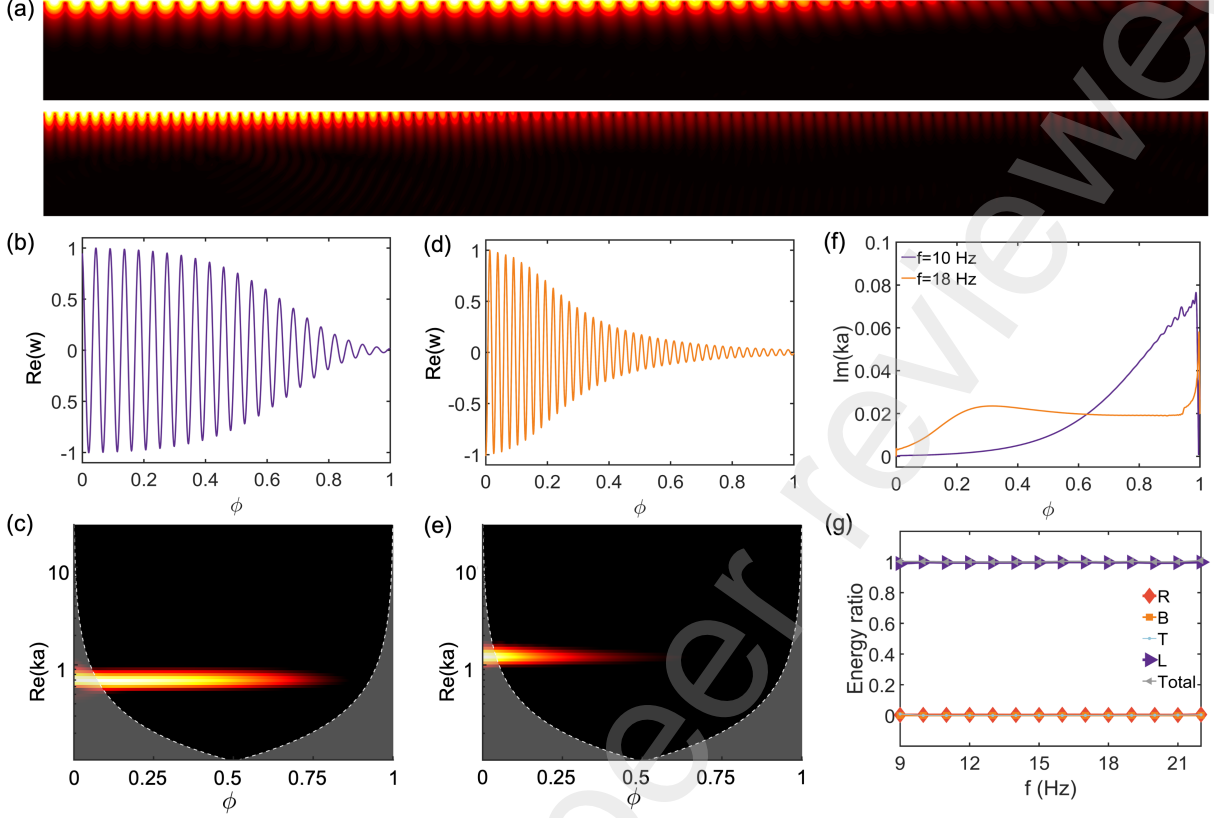


Figure 12: Verification of adiabatic evolution of Rayleigh waves in the frequency domain. (a) Frequency response of the Rayleigh wave under excitation from Eq. (18) at frequencies of 10 Hz (top panel) and 18 Hz (bottom panel). (b) The real part of vertical displacement distribution w along the cross-section at $z = -3$ m, shown in the top panel of (a). (c) Wavelet transforms of the data from (b). (d) The real part of vertical displacement distribution w along the cross-section at $z = -3$ m, depicted in the bottom panel of (a). (e) Wavelet transforms of the data from (d). (f) Local wavenumber function in relation to the normalized spatial coordinate ϕ . (g) Energy ratios of the reflected Rayleigh wave, transmitted Rayleigh wave, transferred bulk wave, energy dissipation within the EDM, and the total incident Rayleigh wave energy.

442 Hz, aligning well with the results in Fig. 11(d) from local unit cell analysis. To extract the
443 decay factor $\text{Im}(k)$ at different positions, we use the following

$$\text{Im}(k(x)) = \frac{d}{dx} \ln \left(\frac{|w(x)|}{|w(0)|} \right), \quad (23)$$

444 where $|w(x)|$ is the magnitude of w displacement field at $z = 3$ m, $|w(0)|$ is the magnitude
445 of w displacement at $z = 3$ m and $x = 0$ m, and the derivative is calculated by the finite
446 difference method.

447 The decay factors for the Rayleigh wave at excitation frequencies of 10 Hz and 18 Hz
448 are shown in Fig. 12(f). At 10 Hz, the decay factor is small and increases slowly when
449 $\phi < 0.5$, but rises rapidly and becomes significant when $\phi > 0.5$. At 18 Hz, the decay
450 factor increases to 0.2 after a short distance $\phi = 0.2$, and then remains constant, indicating
451 exponential decay when $\phi > 0.2$. In addition, it can be observed that the decay factors in

452 Fig. 12(f) agree well with those in Fig. 11(f), demonstrating that the decaying behavior
 453 of Rayleigh waves can be precisely predicted by a local unit analysis. It is important to
 454 note that the agreement between frequency response and unit cell analysis is valid only
 455 for systems that satisfy the adiabatic conditions. This coincidence verifies that the system
 456 satisfies the adiabatic conditions *a posteriori*. The resulting perfect energy dissipation proves
 457 its potential as a broadband Rayleigh wave absorber. As shown in Fig. 12(a), the Rayleigh
 458 wave is perfectly absorbed by the slowly varying EDM at both 10 Hz and 18 Hz. Finally, we
 459 perform an energy analysis of this system. The energy ratios for different waves at various
 460 frequencies are calculated as per the method in Section 2, shown in Fig. 12(g). From 9 Hz
 461 to 22 Hz, the energy ratio absorbed by resonators equals the incident energy ratio, while
 462 the energy ratios of other waves remain zero. Thus, this Rayleigh wave absorber operates
 463 perfectly over a broad frequency range.

464 Next, we turn to discussing the Rayleigh wave behavior in the time domain. For the
 465 excitation frequencies of 10 Hz and 18 Hz, the corresponding time evolution processes from
 466 initial time 0 to end time t_e are shown in Figs. 13(a) and 13(b), respectively. A Rayleigh
 467 wave in the time domain is excited by a distributed line displacement load at $x = 0$ with
 468 the profile

$$u = (re^{-kqz} + 2sqe^{-ksz}) g(t), \quad (24a)$$

$$w = q (re^{-kqz} - 2e^{-ksz}) g\left(t - \frac{1}{4f}\right), \quad (24b)$$

469 where $g(t)$ is a 10-cycles tone-burst signal defined as $g(t) = H\left(t - \frac{10}{f}\right) [1 - \cos\left(\frac{2\pi ft}{10}\right)] \sin(2\pi ft)$
 470 with excitation frequency $f = 10$ Hz, and $H(t)$ is the Heaviside step function. In Fig. 13, we
 471 observe that the Rayleigh waves decay gradually without generating any reflected Rayleigh
 472 waves or scattered bulk waves at both frequencies. This verifies that our system can function
 473 as an effective Rayleigh wave absorber. Additionally, the wavelength of the Rayleigh wave
 474 remains nearly constant across different positions, consistent with the results shown in Figs.
 475 11(c) and 11(e). The Rayleigh wave decays slowly at 10 Hz and rapidly at 18 Hz, but in
 476 both cases, it fully decays upon reaching the right boundary.

477 5.3. Applications of slowly space-varying EDMs

478 Based on the previous results of Rayleigh wave propagation in slowly space-varying
 479 EDMs, we propose two applications. The first application is a boundary absorber designed
 480 for surface acoustic wave (SAW) devices. In traditional SAW devices, interdigital transducers
 481 generate and receive Rayleigh wave signals, but reflected Rayleigh waves from boundaries
 482 can adversely affect device performance. To mitigate these unwanted reflected waves, two
 483 space-varying EDMs, each consisting of 100 unit cells, are aligned in opposite directions. The
 484 function of side length l with respect to the normalized spatial coordinate ϕ for a boundary
 485 absorber is shown in the left panel of Fig. 14(a), where $l = 0$ means no resonators are
 486 attached. According to the previous results, the Rayleigh wave can be perfectly absorbed
 487 at the boundaries over a broad frequency range. To verify the results, we perform the FEM
 488 analysis in the frequency domain. A displacement load described in Eq. (24) is applied in

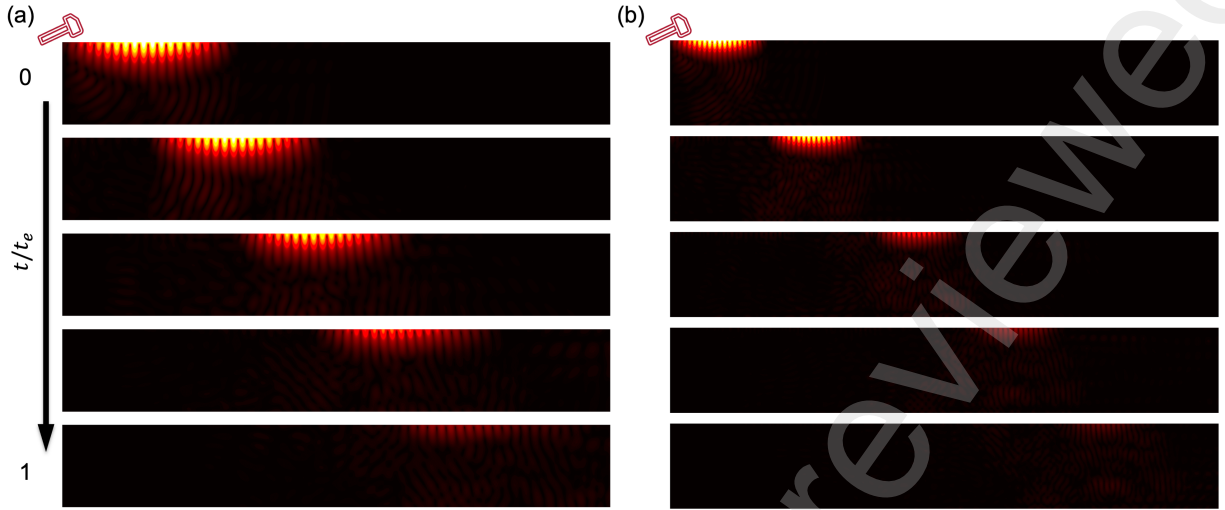


Figure 13: Verification of adiabatic evolution of Rayleigh waves in the time domain: (a) At 10 Hz. (b) At 18 Hz.

489 the middle. For a 10 Hz excitation, the 2D frequency response is depicted in the top panel in
 490 Fig. 14(b), and the displacement field at $z = 3$ m is described in the left panel of Fig. 14(c).
 491 The results demonstrate that the Rayleigh wave is absorbed effectively at this frequency.

492 The second application is a Rayleigh wave amplitude modulator, which features a cone-
 493 shaped EDM attached to the center of the substrate. The function of l with respect to ϕ for
 494 the Rayleigh wave amplitude modulator is shown in the right panel of Fig. 14(a). The same
 495 loading is applied on the left side of the substrate. For an excitation frequency of 10 Hz, the
 496 2D frequency response is shown in the bottom panel of Fig. 14(b), and the displacement
 497 field at $z = 3$ m is illustrated in the right panel of Fig. 14(c). Here, the maximum side
 498 length l is set to a small value of 0.3, so the Rayleigh wave cannot be completely attenuated
 499 to zero but can be reduced to a finite value. By adjusting the maximum value of l , different
 500 output amplitudes of the Rayleigh wave can be achieved. Additionally, the introduction
 501 of active devices can enable time-dependent adjustments of stiffness, mass, and damping,
 502 allowing for real-time modulation of the Rayleigh wave.

503 6. Conclusion

504 In this study, we propose a novel EDM to effectively mitigate low-frequency broadband
 505 Rayleigh waves and their scattered components. Initially, we incorporate a single resonator
 506 array within the EDM to achieve Rayleigh wave mitigation over a narrow frequency range.
 507 However, the introduction of the EDM induced scattered waves and energy dissipation,
 508 prompting us to develop a comprehensive energy analysis framework to quantify the contrib-
 509 utions of each wave component. This analysis provides critical insights for optimizing EDM
 510 design and improving wave control strategies. To address broader applications, we extend
 511 the design to incorporate multiple resonators, achieving subwavelength-scale, broadband,
 512 and low-frequency Rayleigh wave mitigation. Further, we introduce a slowly space-varying

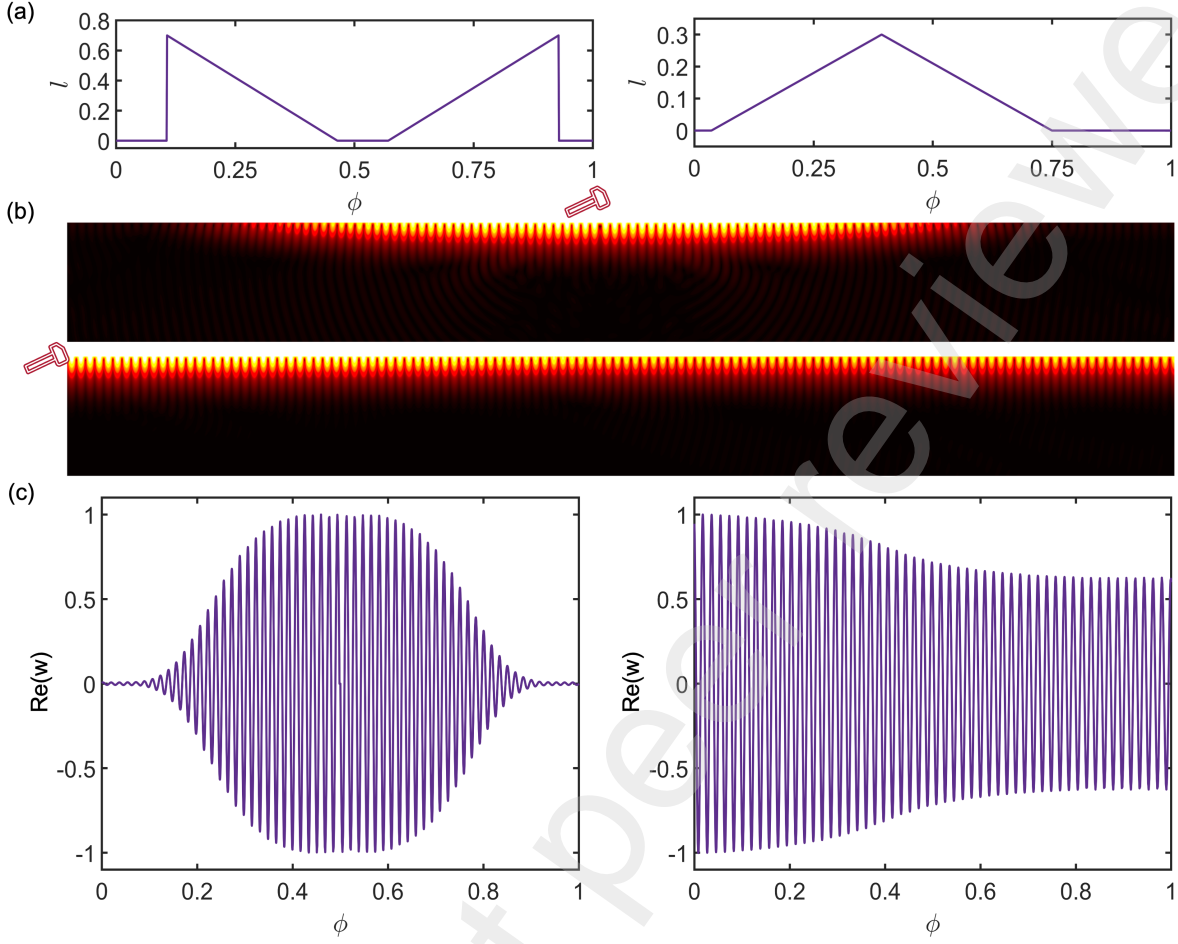


Figure 14: Application of slowly space-varying EDMs as a perfect boundary absorber and a Rayleigh wave amplitude modulator. (a) Variation of the side length of the resonator l as a function of the normalized spatial coordinate ϕ for a boundary absorber (left) and an amplitude modulator (right). (b) Frequency response of the boundary absorber (top) and the amplitude modulator (bottom) under excitation described by Eq. (18) at a frequency of 10 Hz. (c) In the left (right) panel, the real part of vertical displacement distribution w , along the cross-section at $z = -3$ m of the boundary absorber (amplitude modulator), shown in the top (bottom) panel of (b).

513 EDM to eliminate scattered waves, enabling perfect Rayleigh wave absorption across a broad
 514 frequency range. Given the lack of established theories for wave behavior in such systems, we
 515 propose a local unit cell analysis method based on the adiabatic theorem, allowing precise
 516 predictions of wave evolution and facilitating innovative designs, such as perfect rainbow
 517 absorbers and Rayleigh wave modulators. These findings highlight the significant potential
 518 of EDMs in advancing wave control and vibration suppression for engineering applications.
 519 Despite these advancements, challenges remain. For instance, achieving perfect rainbow
 520 absorption under adiabatic conditions often requires a large number of resonators, leading
 521 to material inefficiency. Although the adiabatic condition is not strictly necessary, alter-
 522 native approaches such as the theory of shortcut to adiabaticity [64] could mitigate these

523 constraints. Furthermore, determining the minimal EDM length required for perfect absorp-
524 tion beyond adiabatic conditions poses an open question. For perfect absorption beyond the
525 adiabatic conditions, an absorption inequality suggests that the EDM length must exceed
526 a certain threshold determined by a length function related to the resonator parameters,
527 based on the principles of causality and the Kramers-Kronig relationship [65, 66]. Absorp-
528 tion inequalities derived in acoustics and electrodynamics suggest a lower bound related to
529 resonator parameters, but their adaptation to surface wave systems remains unexplored and
530 warrants further study. In conclusion, this study establishes a foundation for the practical
531 application of EDMs in wave mitigation and provides a pathway for future research to refine
532 these systems for enhanced efficiency and broader applicability.

533 CRediT authorship contribution statement

534 **Siqi Wang:** Writing – original draft, Methodology, Writing – review & editing, Formal
535 Analysis, Conceptualization, Validation. **Zhigang Cao:** Writing – review & editing, Con-
536 ceptualization, Methodology, Supervision, Funding acquisition. **Shaoyun Wang:** Writing –
537 original draft, Writing – review & editing, Methodology, Formal Analysis, Conceptualization,
538 Validation. **Qian Wu:** Writing – review & editing, Writing – original draft, Methodology,
539 Conceptualization, Validation. **Jiaji Chen:** Writing – review & editing, Validation. **Yuan-
540 qiang Cai:** Writing – review & editing, Supervision. **Guoliang Huang:** Writing – review
541 & editing, Writing – original draft, Conceptualization, Supervision.

542 Declaration of competing interest

543 The authors declare that there are no competing financial interests or personal relation-
544 ships that could have influenced the work reported in this paper.

545 Data availability

546 No data was used for the research described in the article.

547 Acknowledgements

548 The work is supported by the National Natural Science Foundation of China (No.
549 51978611), the Science Fund for Distinguished Young Scholars of Zhejiang Province (No.
550 LR21E080004), and the Center for Balance Architecture, Zhejiang University. The authors
551 sincerely thank Dr. Yanzheng Wang for his valuable feedback and constructive suggestions,
552 which greatly improved the quality of this paper.

553 Appendix A

554 The resultant of two polynomials $f(x) = a_nx^n + \dots + a_0$, $g(x) = b_mx^m + \dots + b_0$, $a_n \neq 0$,
555 $b_n \neq 0$, $n > 0$, $m > 0$ equals to the determinant of their Sylvester matrix, namely

$$\text{Res}(f, g) = \det[\text{Syl}(f, g)],$$

556 where Sylvester matrix of two polynomials f, g is defined by

$$\text{Syl}(f, g) = \begin{bmatrix} a_n & a_{n-1} & a_{n-2} & \cdots & 0 & 0 & 0 \\ 0 & a_n & a_{n-1} & \cdots & 0 & 0 & 0 \\ \vdots & \vdots & \vdots & \ddots & \vdots & \vdots & \vdots \\ 0 & 0 & 0 & \cdots & a_1 & a_0 & 0 \\ 0 & 0 & 0 & \cdots & a_2 & a_1 & a_0 \\ b_m & b_{m-1} & b_{m-2} & \cdots & 0 & 0 & 0 \\ 0 & b_m & b_{m-1} & \cdots & 0 & 0 & 0 \\ \vdots & \vdots & \vdots & \ddots & \vdots & \vdots & \vdots \\ 0 & 0 & 0 & \cdots & b_1 & b_0 & 0 \\ 0 & 0 & 0 & \cdots & b_2 & b_1 & b_0 \end{bmatrix},$$

557 where a_n, \dots, a_0 are the coefficients of f and b_m, \dots, b_0 are the coefficients of g .

558 The resultant can be used to solve polynomial equations. For equations

$$\begin{cases} 5x^2 - 6xy + 5y^2 - 16 = 0, \\ 2x^2 - (1+y)x + y^2 - y - 4 = 0. \end{cases}$$

559 We define polynomials $f(x) = 5x^2 - 6xy + 5y^2 - 16$, $g(x) = 2x^2 - (1+y)x + y^2 - y - 4$.

560 Then we eliminate variable x , and we have

$$\text{Res}(f, g) = \begin{vmatrix} 5 & -6y & 5y^2 - 16 & 0 \\ 0 & 5 & -6y & 5y^2 - 16 \\ 2 & -(1+y) & y^2 - y - 4 & 0 \\ 0 & 2 & -(1+y) & y^2 - y - 4 \end{vmatrix} = 32(y-2)(y-1)(y+1)^2.$$

561 The vanishment of resultant gives the solution $y = 2$, or $y = 1$, or $y = -1$.

562 When $y = 2$, the original equations are reduced as

$$\begin{cases} 5x^2 - 12x + 4 = 0, \\ 2x^2 - 3x - 2 = 0, \end{cases}$$

563 with the root of $x = 2$. Similarly, the root $x = -1$ for $y = 1$ whereas the root $x = 1$ for
564 $y = -1$.

565 References

- 566 [1] Z. Liu, X. Zhang, Y. Mao, Y. Y. Zhu, Z. Yang, C. T. Chan, P. Sheng, Locally resonant sonic materials,
567 science 289 (5485) (2000) 1734–1736.
- 568 [2] Q. Wu, X. Xu, H. Qian, S. Wang, R. Zhu, Z. Yan, H. Ma, Y. Chen, G. Huang, Active metamateri-
569 als for realizing odd mass density, Proceedings of the National Academy of Sciences 120 (21) (2023)
570 e2209829120.
- 571 [3] M. I. Hussein, M. J. Leamy, M. Ruzzene, Dynamics of phononic materials and structures: Historical
572 origins, recent progress, and future outlook, Applied Mechanics Reviews 66 (4) (2014) 040802.

- 573 [4] S. A. Cummer, J. Christensen, A. Alù, Controlling sound with acoustic metamaterials, *Nature Reviews Materials* 1 (3) (2016) 1–13.
- 574 [5] Y. F. Wang, Y. Z. Wang, B. Wu, W. Chen, Y.-S. Wang, Tunable and active phononic crystals and
575 metamaterials, *Applied Mechanics Reviews* 72 (4) (2020) 040801.
- 576 [6] H. Huang, C. Sun, G. Huang, On the negative effective mass density in acoustic metamaterials, *International
577 Journal of Engineering Science* 47 (4) (2009) 610–617.
- 578 [7] X. Zhou, X. Liu, G. Hu, Elastic metamaterials with local resonances: an overview, *Theoretical and
579 Applied Mechanics Letters* 2 (4) (2012) 041001.
- 580 [8] S. H. Lee, O. B. Wright, Origin of negative density and modulus in acoustic metamaterials, *Physical
581 Review B* 93 (2) (2016) 024302.
- 582 [9] R. Zhu, X. Liu, G. Hu, C. Sun, G. Huang, Negative refraction of elastic waves at the deep-subwavelength
583 scale in a single-phase metamaterial, *Nature communications* 5 (1) (2014) 5510.
- 584 [10] A. Sukhovich, L. Jing, J. H. Page, Negative refraction and focusing of ultrasound in two-dimensional
585 phononic crystals, *Physical Review B—Condensed Matter and Materials Physics* 77 (1) (2008) 014301.
- 586 [11] N. Contreras, X. Zhang, H. Hao, F. Hernández, Application of elastic metamaterials/meta-structures
587 in civil engineering: A review, *Composite Structures* 327 (2024) 117663.
- 588 [12] G. W. Milton, M. Briane, J. R. Willis, On cloaking for elasticity and physical equations with a trans-
589 formation invariant form, *New journal of physics* 8 (10) (2006) 248.
- 590 [13] H. Nassar, Y. Chen, G. Huang, Polar metamaterials: a new outlook on resonance for cloaking applica-
591 tions, *Physical review letters* 124 (8) (2020) 084301.
- 592 [14] M. Farhat, S. Guenneau, S. Enoch, Ultrabroadband elastic cloaking in thin plates, *Physical review
593 letters* 103 (2) (2009) 024301.
- 594 [15] X. Zhang, Z. Liu, Superlenses to overcome the diffraction limit, *Nature materials* 7 (6) (2008) 435–441.
- 595 [16] X. Zhou, G. Hu, Superlensing effect of an anisotropic metamaterial slab with near-zero dynamic mass,
596 *Applied Physics Letters* 98 (26) (2011).
- 597 [17] R. Zhu, X. Liu, G. Hu, C. Sun, G. Huang, A chiral elastic metamaterial beam for broadband vibration
598 suppression, *Journal of Sound and Vibration* 333 (10) (2014) 2759–2773.
- 599 [18] Y. Xiao, J. Wen, D. Yu, X. Wen, Flexural wave propagation in beams with periodically attached vibra-
600 tion absorbers: Band-gap behavior and band formation mechanisms, *Journal of Sound and Vibration*
601 332 (4) (2013) 867–893.
- 602 [19] J. Lou, H. Fan, J. Yang, M. Xu, J. Du, Metamaterial design enabling simultaneous manipulation of
603 rayleigh and love waves, *Thin-Walled Structures* 204 (2024) 112273.
- 604 [20] Y. Zeng, Y. Xu, H. Yang, M. Muzamil, R. Xu, K. Deng, P. Peng, Q. Du, A matryoshka-like seismic
605 metamaterial with wide band-gap characteristics, *International Journal of Solids and Structures* 185
606 (2020) 334–341.
- 607 [21] A. Alzawi, M. H. El Naggar, Full scale experimental study on vibration scattering using open and
608 in-filled (geofoam) wave barriers, *Soil Dynamics and Earthquake Engineering* 31 (3) (2011) 306–317.
- 609 [22] Z. Cao, Y. Cai, Isolation of train-induced ground-borne vibration by trenches on a poroelastic half-
610 space, *Journal of Engineering Mechanics* 139 (5) (2013) 580–593.
- 611 [23] D. Ulgen, O. Toygar, Screening effectiveness of open and in-filled wave barriers: a full-scale experimental
612 study, *Construction and Building Materials* 86 (2015) 12–20.
- 613 [24] X. Pu, Z. Shi, Broadband surface wave attenuation in periodic trench barriers, *Journal of Sound and
614 Vibration* 468 (2020) 115130.
- 615 [25] D. Thompson, J. Jiang, M. Toward, M. Hussein, E. Ntotsios, A. Dijckmans, P. Coulier, G. Lombaert,
616 G. Degrande, Reducing railway-induced ground-borne vibration by using open trenches and soft-filled
617 barriers, *Soil Dynamics and Earthquake Engineering* 88 (2016) 45–59.
- 618 [26] D. J. Thompson, G. Kouroussis, E. Ntotsios, Modelling, simulation and evaluation of ground vibration
619 caused by rail vehicles, *Vehicle System Dynamics* 57 (7) (2019) 936–983.
- 620 [27] Y. Xu, X. Pu, A. Palermo, A. Marzani, Y. Cai, Z. Cao, An analytical formulation to model geometric
621 and resonant scattering of buried metabarriers for traffic-induced vibrations mitigation, *International
622 Journal of Solids and Structures* 270 (2023) 112237.

- 624 [28] Y.-Q. Cai, G.-Y. Ding, C.-J. Xu, Amplitude reduction of elastic waves by a row of piles in poroelastic
625 soil, *Computers and Geotechnics* 36 (3) (2009) 463–473.
- 626 [29] G. M. Álamo, J. D. Bordón, J. J. Aznarez, G. Lombaert, The effectiveness of a pile barrier for vibration
627 transmission in a soil stratum over a rigid bedrock, *Computers and Geotechnics* 110 (2019) 274–286.
- 628 [30] S. Brûlé, E. Javelaud, S. Enoch, S. Guenneau, Experiments on seismic metamaterials: molding surface
629 waves, *Physical review letters* 112 (13) (2014) 133901.
- 630 [31] L. Meng, Z. Cheng, Z. Shi, Vibration mitigation in saturated soil by periodic pile barriers, *Computers*
631 and *Geotechnics* 117 (2020) 103251.
- 632 [32] S. Wang, Z. Cao, Y. Xu, Z. Xiao, Z. Yuan, Y. Cai, C. Gou, Prediction and mitigation of train-induced
633 vibrations of over-track buildings on a metro depot: Field measurement and numerical simulation,
634 *Journal of Vibration and Control* 29 (23-24) (2023) 5413–5426.
- 635 [33] T. Sheng, G. B. Liu, X. C. Bian, W. X. Shi, Y. Chen, Development of a three-directional vibration
636 isolator for buildings subject to metro-and earthquake-induced vibrations, *Engineering Structures* 252
637 (2022) 113576.
- 638 [34] D. Colquitt, A. Colombi, R. Craster, P. Roux, S. Guenneau, Seismic metasurfaces: Sub-wavelength
639 resonators and rayleigh wave interaction, *Journal of the Mechanics and Physics of Solids* 99 (2017)
640 379–393.
- 641 [35] H. Zheng, L. Miao, P. Xiao, K. Lei, Q. Wang, Novel metamaterial foundation with multi low-frequency
642 bandgaps for isolating earthquakes and train vibrations, in: *Structures*, Vol. 61, Elsevier, 2024, p.
643 106070.
- 644 [36] R. Cai, Y. Jin, B. Djafari-Rouhani, S. Zhou, P. Chen, T. Rabczuk, H. Zhu, X. Zhuang, Attenuation
645 of rayleigh and pseudo surface waves in saturated soil by seismic metamaterials, *Computers and*
646 *Geotechnics* 165 (2024) 105854.
- 647 [37] X. Pu, A. Palermo, Z. Cheng, Z. Shi, A. Marzani, Seismic metasurfaces on porous layered media: Surface
648 resonators and fluid-solid interaction effects on the propagation of rayleigh waves, *International Journal*
649 *of Engineering Science* 154 (2020) 103347.
- 650 [38] C. He, S. Zhou, X. Li, H. Di, X. Zhang, Forest trees as a natural metamaterial for surface wave
651 attenuation in stratified soils, *Construction and Building Materials* 363 (2023) 129769.
- 652 [39] Z. Chen, G. Wang, C. Lim, Artificially engineered metaconcrete with wide bandgap for seismic surface
653 wave manipulation, *Engineering Structures* 276 (2023) 115375.
- 654 [40] A. Ni, Z. Shi, Q. Meng, Broadband surface wave attenuation in porous soil by elastic metasurfaces,
655 *International Journal of Mechanical Sciences* 264 (2024) 108838.
- 656 [41] Y. Xu, Z. Cao, K. Cui, Y. Cai, X. Pu, Tunable metasurfaces for seismic love wave manipulation: A
657 theoretical study, *International Journal of Mechanical Sciences* 251 (2023) 108327.
- 658 [42] A. Palermo, B. Yousefzadeh, C. Daraio, A. Marzani, Rayleigh wave propagation in nonlinear metasur-
659 faces, *Journal of Sound and Vibration* 520 (2022) 116599.
- 660 [43] J. Lou, X. Fang, H. Fan, J. Du, A nonlinear seismic metamaterial lying on layered soils, *Engineering*
661 *Structures* 272 (2022) 115032.
- 662 [44] B. Zhao, H. R. Thomsen, X. Pu, S. Fang, Z. Lai, B. Van Damme, A. Bergamini, E. Chatzi, A. Colombi,
663 A nonlinear damped metamaterial: Wideband attenuation with nonlinear bandgap and modal dissipation,
664 *Mechanical Systems and Signal Processing* 208 (2024) 111079.
- 665 [45] X. Fang, J. Lou, Y. M. Chen, J. Wang, M. Xu, K. C. Chuang, Broadband rayleigh wave attenuation
666 utilizing an inertant seismic metamaterial, *International Journal of Mechanical Sciences* 247 (2023)
667 108182.
- 668 [46] G. Huang, C. Sun, Band gaps in a multiresonator acoustic metamaterial (2010).
- 669 [47] Y. Chen, M. V. Barnhart, J. Chen, G. Hu, C. Sun, G. Huang, Dissipative elastic metamaterials for
670 broadband wave mitigation at subwavelength scale, *Composite Structures* 136 (2016) 358–371.
- 671 [48] M. V. Barnhart, X. Xu, Y. Chen, S. Zhang, J. Song, G. Huang, Experimental demonstration of a
672 dissipative multi-resonator metamaterial for broadband elastic wave attenuation, *Journal of Sound and*
673 *Vibration* 438 (2019) 1–12.
- 674 [49] X. Pu, A. Marzani, A. Palermo, A multiple scattering formulation for elastic wave propagation in

- space–time modulated metamaterials, *Journal of Sound and Vibration* 573 (2024) 118199.
- [50] J. Santini, X. Pu, A. Palermo, F. Braghin, E. Riva, Controlling surface acoustic waves (saws) via temporally graded metasurfaces, Available at SSRN 4774810 (2024).
- [51] A. Palermo, P. Celli, B. Yousefzadeh, C. Daraio, A. Marzani, Surface wave non-reciprocity via time-modulated metamaterials, *Journal of the Mechanics and Physics of Solids* 145 (2020) 104181.
- [52] Q. Wu, H. Chen, H. Nassar, G. Huang, Non-reciprocal rayleigh wave propagation in space–time modulated surface, *Journal of the Mechanics and Physics of Solids* 146 (2021) 104196.
- [53] Q. Wu, X. Zhang, P. Shivashankar, Y. Chen, G. Huang, Independent flexural wave frequency conversion by a linear active metalayer, *Physical Review Letters* 128 (24) (2022) 244301.
- [54] E. Riva, M. I. Rosa, M. Ruzzene, Edge states and topological pumping in stiffness-modulated elastic plates, *Physical Review B* 101 (9) (2020) 094307.
- [55] M. I. Rosa, R. K. Pal, J. R. Arruda, M. Ruzzene, Edge states and topological pumping in elastic lattices with periodically modulated coupling, *arXiv preprint arXiv:1811.02637* (2018).
- [56] H. Chen, H. Zhang, Q. Wu, Y. Huang, H. Nguyen, E. Prodan, X. Zhou, G. Huang, Creating synthetic spaces for higher-order topological sound transport, *Nature communications* 12 (1) (2021) 5028.
- [57] S. Wang, Z. Hu, Q. Wu, H. Chen, E. Prodan, R. Zhu, G. Huang, Smart patterning for topological pumping of elastic surface waves, *Science Advances* 9 (30) (2023) eadh4310.
- [58] A. Colombi, V. Ageeva, R. J. Smith, A. Clare, R. Patel, M. Clark, D. Colquitt, P. Roux, S. Guenneau, R. V. Craster, Enhanced sensing and conversion of ultrasonic rayleigh waves by elastic metasurfaces, *Scientific Reports* 7 (1) (2017) 6750.
- [59] X. Wu, Z. Wen, Y. Jin, T. Rabczuk, X. Zhuang, B. Djafari-Rouhani, Broadband rayleigh wave attenuation by gradient metamaterials, *International Journal of Mechanical Sciences* 205 (2021) 106592.
- [60] S. J. Mitchell, A. Pandolfi, M. Ortiz, Metaconcrete: designed aggregates to enhance dynamic performance, *Journal of the Mechanics and Physics of Solids* 65 (2014) 69–81.
- [61] R. Das, R. Kumar, S. L. Banerjee, P. P. Kundu, Engineered elastomeric bio-nanocomposites from linseed oil/organoclay tailored for vibration damping, *RSC Advances* 4 (103) (2014) 59265–59274.
- [62] J. Rose, *Ultrasonic Guided Waves in Solid Media*, Cambridge University Press, 2014.
- [63] Y. Long, J. Ren, H. Chen, Intrinsic spin of elastic waves, *Proceedings of the National Academy of Sciences* 115 (40) (2018) 9951–9955.
- [64] D. Guéry-Odelin, A. Ruschhaupt, A. Kiely, E. Torrontegui, S. Martínez-Garaot, J. G. Muga, Shortcuts to adiabaticity: Concepts, methods, and applications, *Reviews of Modern Physics* 91 (4) (2019) 045001.
- [65] H. Y. Mak, X. Zhang, Z. Dong, S. Miura, T. Iwata, P. Sheng, Going beyond the causal limit in acoustic absorption, *Physical Review Applied* 16 (4) (2021) 044062.
- [66] K. N. Rozanov, Ultimate thickness to bandwidth ratio of radar absorbers, *IEEE Transactions on Antennas and Propagation* 48 (8) (2000) 1230–1234.